Nano Research

ISSN 1998-0124 CN 11-5974/O4
https://doi.org/10.26599/NR.2026.94909268

Research Article

A universal NTA chelation-derived strategy to develop triple-functional core@shell magnetic carbon nanorods for microwave absorption, antibacterial, and anticorrosion applications

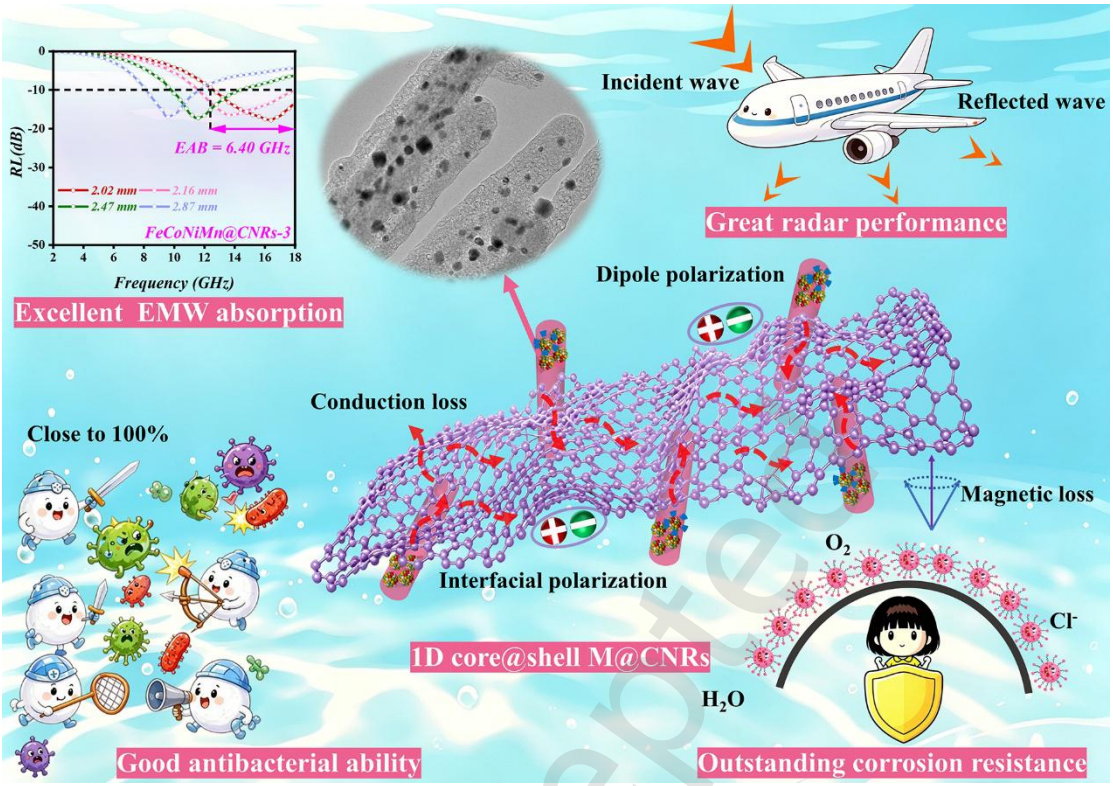
Huirong Li§, Hemin Wang§, Junxiong Xiao, Xin Gao, Beibei Zhan, Xiu Gong, Qiong Peng, Xiaosi Qi(✉)
College of Physics, Guizhou University, Guiyang 550025, China
§ Huirong Li and Hemin Wang contributed equally to this work.

Nano Res., **Just Accepted Manuscript** • https://doi.org/10.26599/NR.2026.94909268
https://www.sciopen.com/journal/1998-0124 on Oct. 17, 2026

© The Authors(s)

Just Accepted

This is a "Just Accepted" manuscript, which has been examined by the peer-review process and has been accepted for publication. A "Just Accepted" manuscript is published online shortly after its acceptance,which is prior to technical editing and formatting and author proofing. Tsinghua University Press (TUP) provides "Just Accepted" as an optional and free service which allows authors to make their results available to the research community as soon as possible after acceptance. After a manuscript has been technically edited and formatted, and the page proofs have been corrected, it will be removed from the "Just Accepted" web site and published officially with volume and article number (e.g., *Nano Research*, **2025**, *18*, 94906990). Please note that technical editing may introduce minor changes to the manuscript text and/or graphics which may affect the content, and all legal disclaimers that apply to the journal pertain. In no event shall TUP be held responsible for errors or consequences arising from the use of any information contained in these "Just Accepted" manuscripts. To cite this anuscript please use its Digital Object Identifier (DOI®),which is identical for all formats of publication.



1D core@shell M@CNRs nanocomposites fabricated via NTAC-based synthesis strategy, designed for achieving microwave absorption, corrosion resistance, and antibacterial properties.

Just Accepted

Research Article

A universal NTA chelation-derived strategy to develop triple-functional core@shell magnetic carbon nanorods for microwave absorption, antibacterial, and anticorrosion applications

Huirong Li[§], Hemin Wang[§], Junxiong Xiao, Xin Gao, Beibei Zhan, Xiu Gong, Qiong Peng, and Xiaosi Qi[*]

College of Physics, Guizhou University, Guiyang 550025, China

[§]Huirong Li and Hemin Wang contributed equally to this work.

Received: 21 September 2026; **Revised:** 14 October 2026; **Accepted:** 17 October 2026

Address correspondence to xsqi@gzu.edu.cn

Cite this article: *Nano Research*, 2026, 19, 94909268 https://doi.org/10.26599/NR.2026.94909268

Just Accepted

Abstract: Simultaneous achievement of high-performance microwave absorption, antibacterial activity, and corrosion resistance remains a key challenge for multifunctional materials in real-world application scenarios. Herein, one-dimensional core@shell FeCo@carbon nanorods (CNRs), FeCoNi@CNRs, and FeCoNiMn@CNRs consisting of magnetic alloy nanoparticles as core confined in the shell of CNRs are fabricated through a nitrilotriacetic acid chelation (NTAC)-assisted hydrothermal route, phenolic-resin coating, and carbonization treatment. The increased annealing temperature promotes graphitization of carbon shell, yielding the improved impedance matching and dielectric/magnetic synergy. The optimized FeCoNi@CNRs deliver a minimum reflection loss of -52.57 dB and an effective absorption bandwidth (EAB) of 5.60 GHz. Successive Ni and Mn incorporation further enhances complex permittivity, attenuation constant, and impedance matching. The acquired FeCoNiMn@CNRs display an EAB of 6.40 GHz, a radar cross-section reduction up to 39.59 $dB \cdot m^2$, a bacteriostatic rate approaching 100% against *E. coli*, and the highest corrosion potential with the lowest corrosion current density in simulated seawater. The functionally complementary core@shell design with magnetic alloy core for loss/ROS generation and graphitic carbon shell for interfacial polarization/barrier protection establishes a facile and universal NTAC-derived strategy for advanced wave-absorbing materials with integrated antibacterial and environmental durability.

Keywords: NTAC-derived strategy, core@shell magnetic CNRs, microwave

Just Accepted

absorption, antibacterial, corrosion resistance

1. Introduction

The exponential proliferation of fifth-generation (5G), radar detection systems and Internet-of-Things (IoT) devices not only bring unprecedented convenience to modern society, but also simultaneously give rise to an omnipresent and increasingly severe electromagnetic (EM) pollution issue [1, 2]. Consequently, microwave absorbing materials (MAMs) have emerged as a critical technological solution, which can convert incident EM energy into thermal dissipation through well-engineered engineered dielectric and magnetic loss mechanisms [3]. Over the past two decades, the design philosophy of MAMs has gradually evolved from the early pursuit of mere "high absorption intensity" to a comprehensive demand for "thin thickness, low density, broad effective absorption bandwidth (EAB), and strong environmental adaptability" [4, 5]. This evolutionary trend has continuously driven the exploration of novel structural configurations and compositional systems, ranging from traditional ferrites and metallic micropowders to advanced carbon-based nanocomposites, emerging two-dimensional material families, and metamaterials [6, 7].

Despite remarkable progress, the field of MAMs still faces several challenges that fundamentally limit the practical deployment of absorbers in real-world scenarios [8, 9]. Firstly, there exists a long-standing trade-off between magnetic loss capability and environmental stability for magnetic MAMs, especially those based on Fe-Co-Ni systems. Their surfaces are highly susceptible to oxidation and acidic/marine corrosion, which rapidly degrades both absorption performance and mechanical

Just Accepted

integrity [10]. Secondly, the majority of existing MAMs are designed with a singular functionality mindset: microwave absorption only. In many practical application scenarios, such as marine vessel anti-corrosion coatings, offshore wind-turbine nacelles, and public electronic enclosures in humid environments, materials are simultaneously exposed to salt-spray corrosion, biofilm colonization by bacteria, and intense EM radiation. Conventional MAMs completely lack intrinsic antibacterial activity and offer little resistance to electrochemical corrosion [11]. Thirdly, achieving a rationally designed multi-scale architecture that synergistically integrates multiple loss mechanisms remains a formidable synthetic challenge. Ideal MAMs should possess a hierarchical architecture where nanoscale building blocks provide polarization centers, mesoscale assemblies extend wave-propagation paths, and macroscale morphologies ensure mechanical robustness [12]. One-dimensional (1D) core@shell nanorods (NRs) represent a particularly attractive geometry because their high aspect ratio facilitates multiple internal reflection and scattering of incident EM waves, while the core@shell heterointerface creates strong interfacial polarization. However, the scalable and composition-tunable fabrication of such 1D architectures with precise spatial control over bimetallic or multimetallic alloy cores remains a significant challenge.

To address these multifaceted challenges, researchers have devoted extensive efforts to exploring various precursor-mediated strategies for fabricating metal/carbon nanocomposites [13]. Metal-organic frameworks (MOFs), covalent organic frameworks (COFs), and coordination polymers gain prominence as sacrificial

Just Accepted

templates due to their uniform porosity and molecular-level metal dispersion [14]. However, most MOF-derived routes are restricted by the limited availability of 1D MOF topologies, complex ligand-exchange or surfactant-assisted growth steps, and poor compositional flexibility when targeting multicomponent transition-metal alloys [15]. Acting as a small, inexpensive, and environmentally benign multidentate chelator bearing one tertiary amine and three carboxylate groups, nitrilotriacetic acid (NTA) offers a refreshingly simple yet powerful alternative [16]. NTA forms extremely stable water-soluble chelates with a broad spectrum of transition-metal ions (Fe^{2+}, Co^{2+}, Ni^{2+}, Mn^{2+}, Cu^{2+}, etc.) through its tripodal coordination geometry, enabling the molecular-level confinement of single or multiple metal species within a single coordination complex [17]. Hydrothermal treatment of such NTA-metal complexes readily yields 1D metal-nitrilotriacetic acid chelate (NTAC) NRs, which serve as ideal 1D precursors for subsequent thermal transformation. Nevertheless, direct carbonization of metal-NTAC often leads to agglomerated metal nanoparticles or collapsed carbon frameworks due to the rapid release of chelated water and structural reorganization at high temperatures [18]. Introducing an intermediate protection layer such as a phenolic resin (PR) shell is critically needed to encapsulate the precursor, buffer the thermal decomposition, and supply an additional carbon source for the in-situ formation of a continuous graphitic carbon nanorods (CNRs) shell [19, 20].

Motivated by the above considerations, this work presents a scalable NTAC-derived strategy for constructing 1D core@shell metal alloy (MA)

Just Accepted

nanoparticles@CNRs (MA=FeCo, FeCoNi, FeCoNiMn) with triply integrated functionalities: high-efficiency microwave absorption, potent antibacterial activity, and superior seawater corrosion resistance. The meticulously designed 1D core@shell MA@CNRs nanocomposite, in which the inner alloy core provides magnetic loss, ROS-mediated antibacterial action, and catalytic activity, while the outer graphitic carbon shell contributes dielectric loss, interfacial polarization, and a physical barrier against corrosive agents, can concurrently deliver outstanding EM wave absorption properties (EMWAPs) (EAB >6.0 GHz), a near-100% bacteriostatic rate, and excellent electrochemical corrosion resistance.

2. Experimental section

2.1 Controllable Production of Metal-NTAC and Metal-NTAC@PR NRs

Typically, different categories of metal-NTAC including FeCo-NTAC, FeCoNi-NTAC and FeCoNiMn-NTAC NRs could be selectively produced by a hydrothermal method. Taking FeCo-NTAC as an example, as summarized in Table S1 (Supporting Information), $CoCl_2 \cdot 6H_2O$, $FeCl_2 \cdot 4H_2O$ and NTA (1.20 g) were dissolved in the mixed solution consisting of water (40 mL) and isopropyl alcohol (30 mL). The resulting solution was stirred continuously for 1.5 h and subjected to subsequent hydrothermal treatment at 180 °C for 7 h. FeCo-NTAC NRs could be acquired after the washed and dried processes. Equally, FeCoNi-NTAC and FeCoNiMn-NTAC NRs were also efficiently fabricated by regulating the kinds of starting reactants (Table S1). Subsequently, the obtained metal-NTAC (200 mg) was ultrasonically dispersed into a mixed solvent containing anhydrous ethanol (210 mL), deionized water (30 mL) and ammonia (9 mL). After the addition of resorcinol (0.4 g) and formaldehyde (0.56 mL), the resulting mixture was magnetically stirred for 24 h. Finally, FeCo-NTAC@PR,

Just Accepted

FeCoNi-NTAC@PR and FeCoNiMn-NTAC@PR could be obtained after the washed and dried treatment, respectively.

2.2 Fabrication of FeCo@CNRs, FeCoNi@CNRs and FeCoNiMn@CNRs

As summarized in Table S2, FeCoNi-NTAC@PR was successively subjected to heat treatment under an argon atmosphere in a tubular furnace at different annealing temperatures (900 °C, 950 °C and 1000 °C) for 2 h. The corresponding samples were labeled as FeCoNi@CNRs-1, FeCoNi@CNRs-2 and FeCoNi@CNRs-3, respectively. Equally, the heat treatment of FeCo-NTAC@PR and FeCoNiMn-NTAC@PR was conducted under an argon atmosphere at 1000 °C for 2 h to yield FeCo@CNRs-3 and FeCoNiMn@CNRs-3 (for easy description), respectively.

3. Results and Discussion

3.1 Microstructure, composition, EM properties, and EMWAPs of FeCoNi@CNRs

Figure 1 provides the schematic diagram for preparing MA@CNRs and microstructures of FeCoNi@CNRs. As described in Figure 1a, NTA serving as an efficient multidentate ligand displays the strong chelation capability toward Fe^{2+}/Co^{2+}/Ni^{2+}/Mn^{2+} because of its abundant tertiary amine and carboxylate groups [21]. And the hydrothermal treatment enables these metal ions to be confined at the molecular level, contributing to the formation of metal-NTAC [22]. Benefiting from the excellent coordination capability of NTA toward various transition-metal ions, this strategy can be universally extended to produce multicomponent metal-NTAC [23, 24]. As displayed in Figure 1b and c, the FeCoNi-NTAC precursor exhibits a typical 1D rod-like morphology with a smooth surface. And the comparison scanning electron microscopy (SEM) investigations (Figure 1b and d) suggest that the acquired NRs after PR coating display the evidently rough surfaces. Typical transmission

Just Accepted

electron microscopy (TEM) observation (Figure 1e) confirms that the FeCoNi-NTAC NRs is fully enwrapped by PR layer, which confirms the formation of core@shell FeCoNi-NTAC@PR NRs [25]. After the heat treatment of FeCoNi-NTAC@PR NRs at 1000 °C, SEM investigation (Figures 1f, S1a and b) reveals that the acquired FeCoNi@CNRs-3 still remains the rod-like morphology with the rough surface. And TEM observation (Figures 1g, S1c and d) verifies that the typical rod-like morphology and core@shell structure of FeCoNi@CNRs-3. Different from FeCoNi-NTAC@PR, TEM image also reveal that abundant black nanoparticles are formed and uniformly embedded throughout the CNRs, displaying a typical core@shell structure. Equally, the typical SEM (Figures S2a-c and S3a-c) and TEM (Figures S2d-f and S3d-f) images confirm that the acquired FeCoNi@CNRs-1 and FeCoNi@CNRs-2 also present the typical rod-like morphology and core@shell structure, which are composed of CNRs as shell and inner black nanoparticles with large quantities as core. And these black nanoparticles should originate from the reduction and alloying of coordinated metal ions during the high-temperature treatment, leading to the generation of FeCoNi alloy nanoparticles confined within the CNRs [26, 27]. As labeled in Figure 1h, three different lattice fringes of ca. 0.18, 0.20 and 0.34 nm are clearly observed in the high-resolution TEM image of FeCoNi@CNRs-3, which are assignable to (200) plane of Ni_3Fe, (110) plane of Co_7Fe_3, and (002) plane of graphitized carbon, respectively [28, 29]. Moreover, the TEM elemental mapping results (Figure 1i and j) of FeCoNi@CNRs-3 reveal that the C element is uniformly distributed throughout the whole nanorod. And Fe, Co and Ni elements are concentrated in the nanoparticle regions and exhibit the highly overlapping distributions, further demonstrating the formation of FeCoNi alloy nanoparticles [30].

Just Accepted

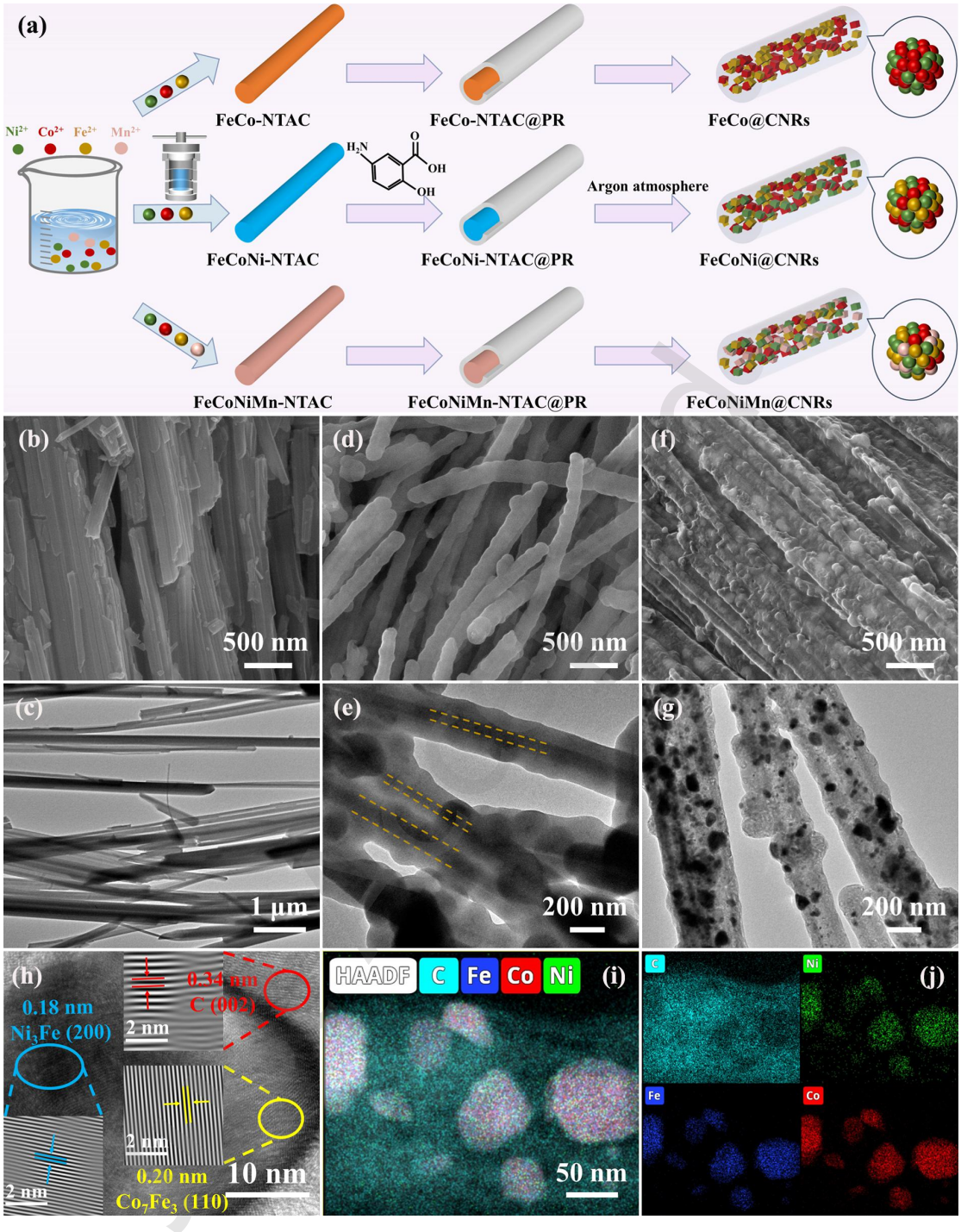


Figure 1. (a) Schematic diagram for preparing multicomponent alloy@CNRs, SEM and TEM images of (b, c) FeCoNi-NTAC, (d, e) FeCoNi-NTAC@PR and (f, g) FeCoNi@CNRs-3, respectively. (h) HRTEM and (i, j) element mapping images for FeCoNi@CNRs-3.

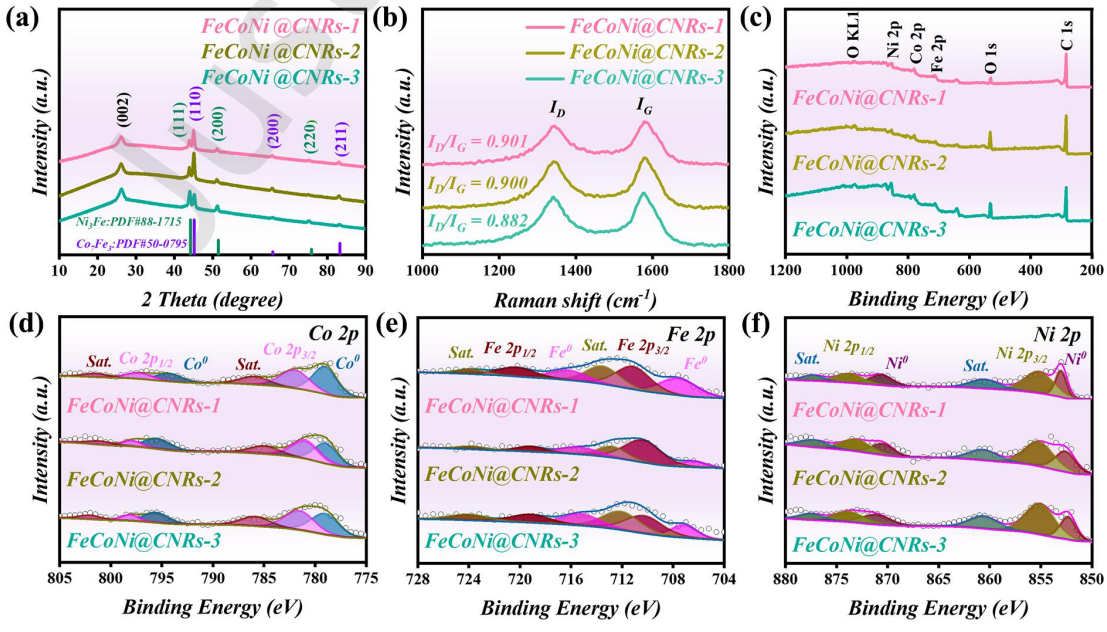
To confirm their compositions, Figure 2 provides the XRD, Raman and XPS spectra for FeCoNi@CNRs samples. As marked in Figure 2a, all the FeCoNi@CNRs

samples carbonized at 900, 950, and 1000 °C exhibit the similar diffraction peaks, indicating their same compositions. And all the marked XRD characteristic peaks can be assigned to (111), (200), and (220) planes of Ni_3Fe alloy (PDF#88-1715), (110), (200), and (211) planes of Co_7Fe_3 (PDF#50-0795), and (002) plane of carbon (PDF#50-0795), respectively [31, 32]. The acquired XRD results are fully consistent with those from HRTEM, which implies that FeCoNi alloy nanoparticles are composed of Ni_3Fe and Co_7Fe_3 phases. The formation of these phase-separated alloys is attributed to the competition between entropy stabilization and enthalpic interactions among different metallic species, which induces the local compositional fluctuations and ultimately drives the phase separation during alloy evolution [33] The Raman spectra (Figure 2b) of FeCoNi@CNRs samples exhibit two characteristic bands at ca. 1339 cm^{-1} and 1579 cm^{-1}, which correspond to the disorder-induced D band and graphitic G band, respectively [34]. And the FeCoNi@CNRs samples display the gradually decreased intensity ratio of these two bands (I_D/I_G)when the carbonization temperature increases from 900 to 1000 °C, indicating a progressively increased degree of graphitization [35]. The enhanced degree of graphitization for carbon-based composites is beneficial for improving the electrical conductivity, thereby promoting the conduction loss and EM wave attenuation [36, 37].

Furthermore, the survey spectra (Figure 2c) of FeCoNi@CNRs samples demonstrate the presence of C, O, Fe, Co, and Ni elements, implying their same elemental compositions. As marked in Figure 2d, all the FeCoNi@CNRs samples display similar Co 2p high-resolution spectra consisting of several characteristic peaks, which correspond to Co^0, Co $2p_{3/2}$, Co $2p_{1/2}$ and their satellite peaks, respectively [38]. Equally, all the Fe 2p (Figure 2e) and Ni 2p (Figure 2f) high-resolution spectra of FeCoNi@CNRs samples are divided into several characteristic peaks assignable to

Just Accepted

Fe^0/Ni^0, Fe $2p_{3/2}$/Ni $2p_{3/2}$, Fe $2p_{1/2}$/Ni $2p_{1/2}$ and their satellite peaks, respectively [39, 40]. Generally, the acquired XPS results demonstrate the generation of Co^0, Fe^0, and Ni^0 in the acquired FeCoNi@CNRs samples. The C 1s high-resolution spectra of FeCoNi@CNRs samples are deconvoluted into three peaks corresponding to C-C/C=C, C-O, and C=O bonds, respectively (Figure S4a) [41]. And XPS quantitative analysis (Figure S4b) clearly shows that the proportion of C-C/C=C bonds steadily increases from 41% to 51% and the contents of C-O and C=O oxygen-containing groups decrease from 47% and 12% to 42% and 7% with the annealing temperature of FeCoNi@CNRs increasing from 900 °C to 1000 °C. The continuous rise in the C-C/C=C ratio reflects a significant improvement in the crystallinity of carbon. In summary, the SEM, TEM, HRTEM, XRD, Raman and XPS results demonstrate that core@shell structure FeCoNi@CNRs consisting of CNRs as the shell, Ni_3Fe and Co_7Fe_3 nanoparticles as the core can be produced in large scale by our proposed route. Generally, the results suggest that the enhanced carbonization temperature contributes to the progressively increased degree of graphitization for FeCoNi@CNRs, which is beneficial to optimize the EM and EMWAPs [42].



Just Accepted

Figure 2. (a) XRD, (b) Raman, (c) survey XPS, and Co 2p, Fe 2p, Ni 2p high resolution XPS spectra for FeCoNi@CNRs samples.

Figure 3 presents the complex permittivity ($\varepsilon = \varepsilon' - i\varepsilon''$), attenuation constant (α), impedance matching (Z), Reflection loss (RL) and EAB results for FeCoNi@CNRs samples. And the ε' (Figure 3a) and ε'' (Figure 3b) values of FeCoNi@CNRs samples exhibit the gradually decreasing tendency within 2-18 GHz, which is attributed to typical frequency-dependent dielectric dispersion [43, 44]. Furthermore, both ε' and ε'' values follow this order: FeCoNi@CNRs-1<FeCoNi@CNRs-2<FeCoNi@CNRs-3, implying that the increased annealing temperature contributes to the boosted values of complex permittivity [45]. The enhanced ε' and ε'' values of FeCoNi@CNRs samples are mainly attributed to the increased graphitization degree and improved electrical transport at the elevated temperature, which facilitate the electron migration and conductive loss [46]. To evaluate the attenuation and impedance matching abilities, the α and Z values of FeCoNi@CNRs samples are calculated by the Equations S1 and S2. The acquired FeCoNi@CNRs samples present the evidently enhanced α values (Figure 3c) with increasing the annealing temperature, indicating their improved EM wave energy dissipation [47]. Equally, the comparison Z values (Figure 3d) also demonstrate the progressively improved impedance matching characteristics of FeCoNi@CNRs samples with the annealing temperature increasing from 900 to 950 and 1000 °C, indicating the efficiently entry of EM waves into FeCoNi@CNRs-3 [48].

To further verify their EM wave absorbing performance, their RL values are calculated by Equation S3. And the minimum RL (RL_{min}) and EAB values of FeCoNi@CNRs-1, FeCoNi@CNRs-2 and FeCoNi@CNRs-3 are -18.02 dB at 6.84 mm and 4.80 GHz at 2.78 mm, -28.84 dB at 7.00 mm and 4.80 GHz at 2.78 mm,

Just Accepted

-52.57 dB at 3.32 mm and 5.60 GHz at 2.23 mm (Figure S5), respectively. As summarized in Figure 3e, the results confirm that the acquired FeCoNi@CNRs present the improved RL_{min} and EAB values with the carbonized temperature increasing from 900 to 950 and 1000 °C, implying the boosted EMWAPs. And the acquired ε_c'' (Figure 3f) and ε_p'' values (Figure 3g) suggest the key contribution of polarization loss [49]. The FeCoNi@CNRs-3 displays much higher ε_c'' and ε_p'' values than those of FeCoNi@CNRs-1 and FeCoNi@CNRs-2, indicating their boosted conductive and polarization loss capacities [50]. On basis of acquired results, the enhancement of polarization loss mainly originates from two aspects: (1) dipole polarization induced by the increased defects with rising the annealing temperature, and (2) interfacial polarization effects resulting from the heterogeneous interfaces between Co_7Fe_3 and Ni_3Fe nanoparticles, as well as the core@shell structures [51]. In summary, the EM, EM wave attenuation and impedance matching characteristics of FeCoNi@CNRs are optimized by modulating the carbonized temperature, which results in their excellent EMWAPs.

Just Accepted

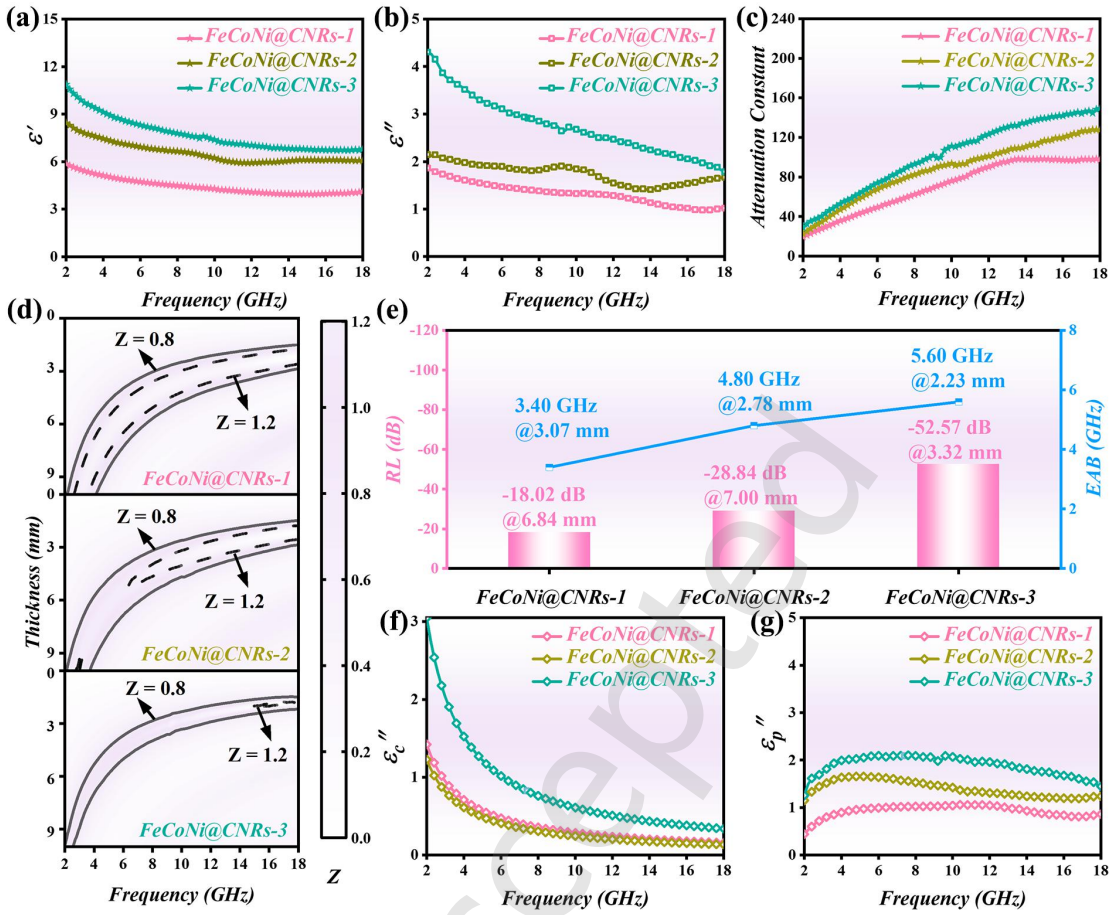


Figure 3. (a) ε', (b) ε'', (c) α, (d) Z (e) summarized RL_{min} and EAB values, (f) $\varepsilon_c'' \sim f$ and (g) $\varepsilon_p'' \sim f$ curves for FeCoNi@CNRs samples.

3.2. Characterization, EM Properties, and EMWAPs of FeCo@CNRs and FeCoNiMn@CNRs

At the annealing temperature of 1000 ℃, FeCo@CNRs and FeCoNiMn@CNRs are also produced to comparatively study the effect of composition on EM parameters and EMWAPs. And the typical TEM images for FeCo-NTAC (Figure 4a) and FeCo-NTAC@PR (Figure 4b) also confirm their typical rod-like morphologies and the uniform encapsulation of PR layer around FeCo-NTAC, which are similar to FeCoNi-NTAC and FeCoNi-NTAC@PR NRs. After the annealing treatment, SEM (Figures S6a and b) and TEM observation (Figures 4c, S6c and d) demonstrate that the acquired FeCo@CNRs-3 still maintains the typical configuration of NRs, which

Just Accepted

are also composed of CNRs as shell and black CoFe nanoparticles as core. And TEM elemental mapping results (Figure 4d) of FeCo@CNRs-3 confirm the uniform distribution of C, and Fe/Co elements across the whole gray nanorod and black nanoparticles. Similar to those of FeCo@CNRs-3 and FeCoNi@CNRs-3, the typical SEM (Figures 4e, S7a and b) and TEM (Figures 4f, S7c and d) investigations also demonstrate that FeCoNiMn@CNRs-3 presents a typical 1D core@shell structure rod-like morphology consisting of black nanoparticles with large quantities and gray nanorod. As labeled in Figure 4g, the clear lattice spacings of 0.21, and 0.19 nm are observed, which should originate from the generated MA [52]. And the lattice spacing of 0.34 nm corresponds to (002) crystal plane of graphitized carbon. Similar to those of FeCo@CNRs-3 and FeCoNi@CNRs-3, the TEM element mapping results of FeCoNiMn@CNRs-3 demonstrate that the uniform distribution of C and Fe/Co/Ni/Mn elements throughout the whole nanorod and inner black nanoparticles.

Just Accepted

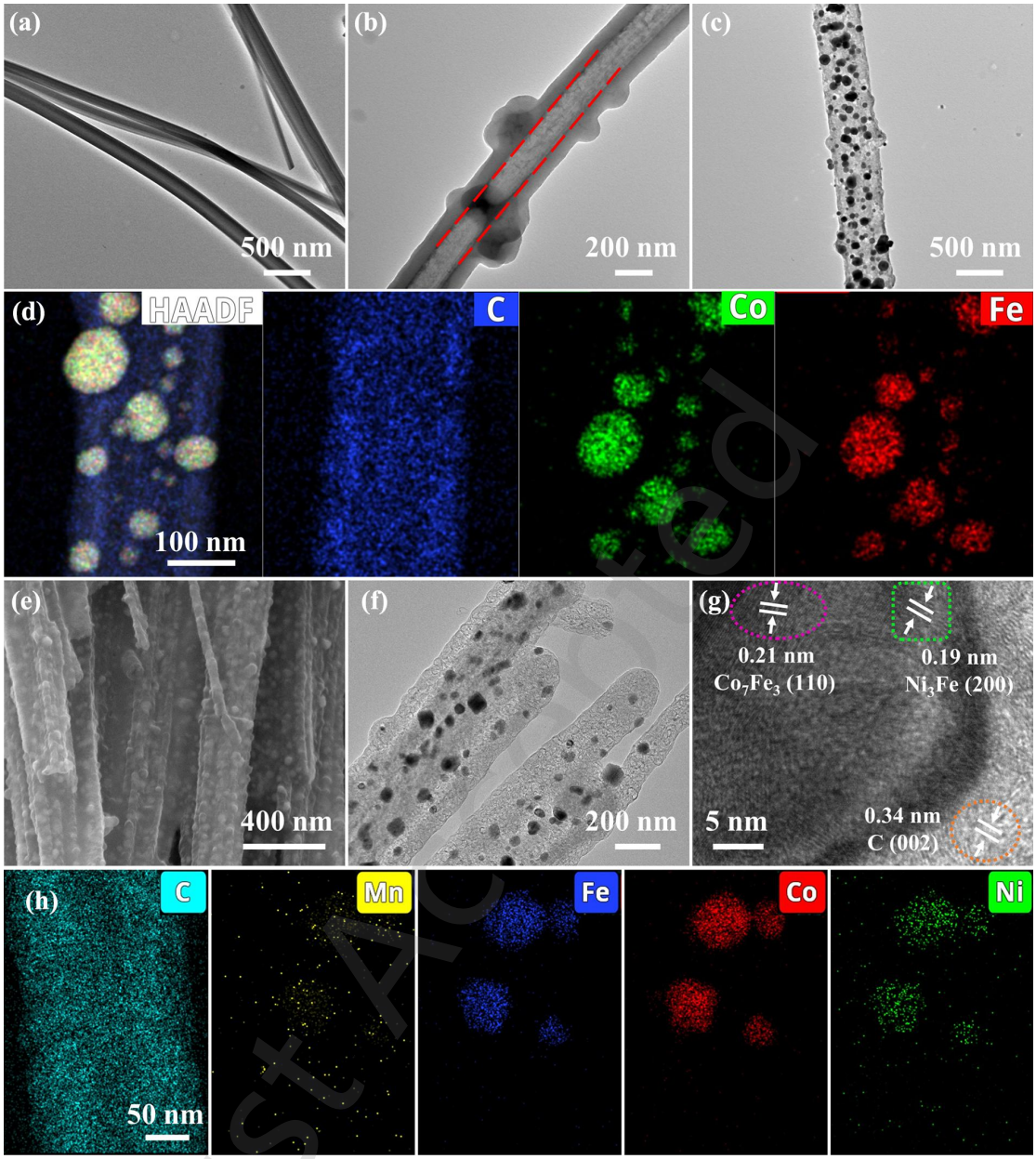


Figure 4. TEM images of (a) FeCo-NTAC, (b) FeCo-NTAC@PR, (c) FeCo@CNRs-3, (d) elemental mapping results of FeCo@CNRs-3, (e-h) SEM, TEM, HRTEM and TEM element mapping images of FeCoNiMn@CNRs-3.

To verify their phases and chemical valence states, Figure 5 gives the XRD, Raman, and XPS spectra of FeCo@CNRs-3 and FeCoNiMn@CNRs-3. The labeled XRD peaks of FeCo@CNRs-3 (Figure 5a) are well matched with graphitized carbon and Co_7Fe_3 (PDF#50-0795). Equally, all the diffraction peaks detected in XRD pattern of FeCoNiMn@CNRs-3 (Figure 5b and c) shift to the lower angles compared with the

Just Accepted

standard diffraction peaks of Ni_3Fe (PDF#88-1715) and Co_7Fe_3 (PDF#50-0795), which is ascribed to the expanded Ni_3Fe and Co_7Fe_3 lattices induced by the incorporation of larger Mn atom [53]. Raman spectroscopy (Figure S8) further elucidates the carbon structural characteristics of FeCo@CNRs-3 and FeCoNiMn@CNRs-3. As marked in Figure 5d, C, O, Fe, and Co elements are detected in FeCo@CNRs-3. The elements of C, O, Fe, Co, Ni, and Mn are observed in FeCoNiMn@CNRs-3, demonstrating the successful incorporation of Mn. Similar to FeCoNi@CNRs samples, the peaks assignable to C=O, C-O, and C-C/C=C bonds are seen in Figure 5e. Notably, the peaks corresponding to Co^0/Fe^0, Co $2p_{3/2}$/Fe $2p_{3/2}$, Co $2p_{1/2}$/Fe $2p_{1/2}$ and their satellite peaks are observed in the Co 2p (Figure 5f) and Fe 2p (Figure 5g) high-resolution spectra of FeCo@CNRs-3 and FeCoNiMn@CNRs-3, respectively [54, 55]. Specifically, compared with FeCo@CNRs-3, both the peaks of Co^0 and Fe^0 for FeCoNiMn@CNRs-3 presents the distinct shift toward the low binding energies (Figure 5f and g). This is because the nucleus's pull on the outermost electrons weakens, making the electron cloud denser [56, 57]. This high electron density state usually brings two positive effects: higher electron mobility means better conductivity, so incoming EM waves can more easily drive electron movement, losing energy in forms like Joule heat, which boosts conductive loss. Having lots of electrons also makes them more likely to accumulate at heterogeneous interfaces, creating stronger interfacial polarization and dissipating EM wave energy, which boosts polarization loss [58]. Furthermore, the Ni 2p (Figure 5g) and Mn 2p (Figure 5i) high-resolution spectra of FeCoNiMn@CNRs-3 consist of several peaks corresponding to Ni^0/Mn^0, Ni $2p_{3/2}$/Mn $2p_{3/2}$, Ni $2p_{1/2}$/Mn $2p_{1/2}$ and their satellite peaks, respectively [59]. Generally, the acquired XRD and XPS results demonstrate

Just Accepted

the formation of FeCo and FeCoNiMn in the acquired FeCo@CNRs-3 and FeCoNiMn@CNRs-3.

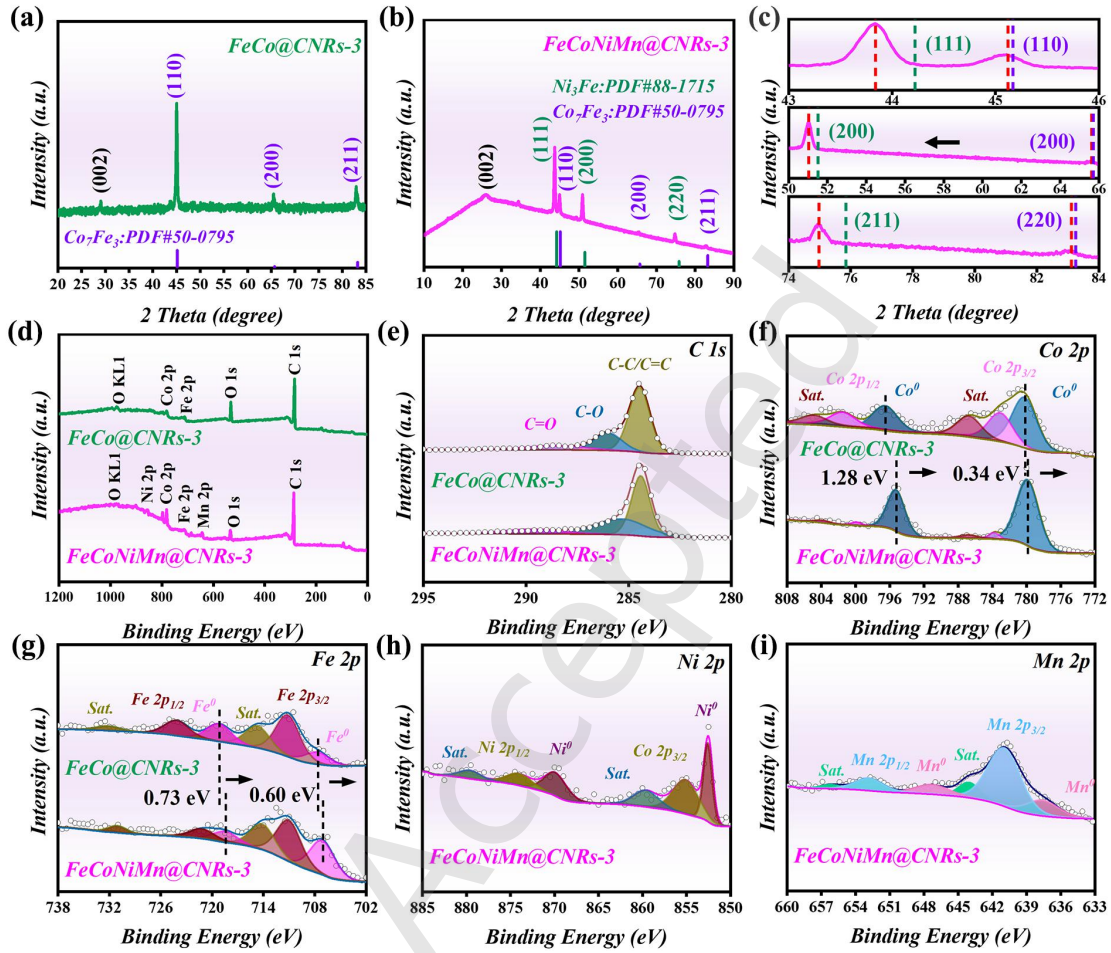


Figure 5. (a-c) XRD, (d-i) survey and high resolution XPS spectra of FeCo@CNRs-3 and FeCoNiMn@CNRs-3.

To further confirm their EM properties and MAPs, Figure 6 provides the complex permittivity, RL diagram, EAB, Z and α of samples. As provided in Figures 3a, 3b, 6a and 6b, the acquired ε' and ε'' values follow the order of FeCo@CNRs-3<FeCoNi@CNRs-3<FeCoNiMn@CNRs-3, implying the evidently boosted complex permittivity. As shown in Figure 6c and d, the FeCo@CNRs-3 and FeCoNiMn@CNRs-3 display the RL_{min} values of -17.65 dB at 9.95 mm, and -19.72 dB at 1.92 mm. As summarized in Figure 6e, the acquired samples from FeCo@CNRs-3 to FeCoNi@CNRs-3 and FeCoNiMn@CNRs-3 present the evidently

Just Accepted

boosted EAB value with the decreased matching thickness. Especially, the EAB value of FeCoNiMn@CNRs-3 reaches the 6.40 GHz at 2.16 mm. As shown in Figure S9, the values of ε_c'' and ε_p'' for FeCoNiMn@CNRs-3 are much higher than those for FeCo@CNRs-3, which implies the significantly improved loss capability. In addition, the Z values of FeCoNiMn@CNRs-3 close to 1 over a wide frequency range, demonstrating its superior impedance matching characteristics compared with FeCo@CNRs-3 and FeCoNi@CNRs-3 (Figure 6f-h). Notably, as smmarized in Figure 6i, the acquired α values are as follows: FeCo@CNRs-3<FeCoNi@CNRs-3<FeCoNiMn@CNRs-3, which indicates the progressively enhanced EM wave attenuation capability [60]. Generally, the acquired outcomes suggest that the successive introduction of Ni and Mn simultaneously improve impedance matching and EM wave attenuation characteristics of FeCo@CNRs, which collectively contribute to the excellent MAPs of FeCoNi@CNRs-3<FeCoNiMn@CNRs-3. More importantly, compared to other representative MAMs (Table S3) [12-15, 20, 31-33, 61-63], the optimized 1D core@shell M@CNRs exhibit significant advantages including low density, strong attenuation capability, wide absorption bandwidth, and a thin matching thickness.

Just Accepted

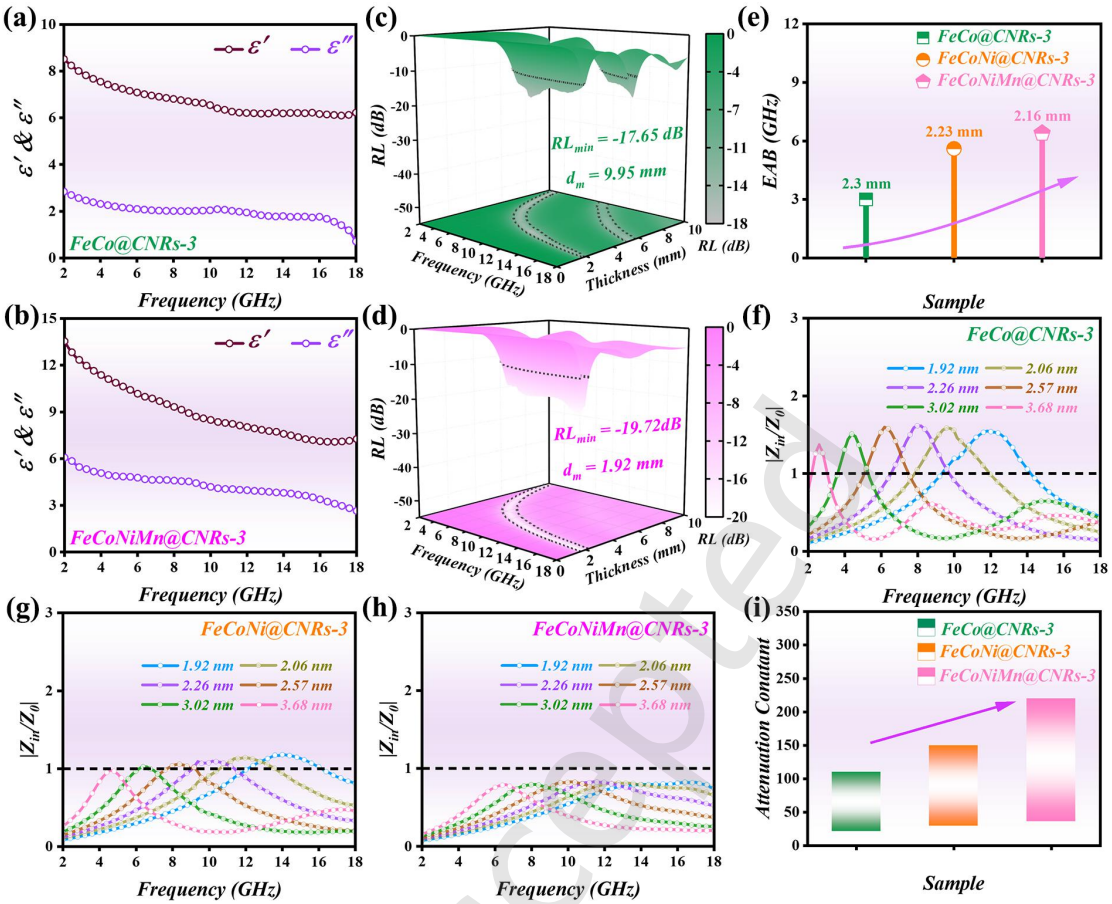


Figure 6. (a, b) Complex permittivity, (c, d) RL diagrams, (e) EAB, (f-h), and (i) α values of FeCo@CNRs-3, FeCoNi@CNRs-3 and FeCoNiMn@CNRs-3.

As shown in Figure 7a, 3D radar cross-section (RCS) spatial scattering distributions of bare PEC substrate and PEC substrates coated with FeCo@CNRs-3, FeCoNi@CNRs-3, FeCoNiMn@CNRs-3 are obtained from CST simulation. The bare PEC substrate exhibits intense specular reflection. After coating with the designed materials, the full-space scattering intensity of targets is significantly suppressed. With the continuous introduction of various metals, the acquired FeCoNiMn@CNRs-3 shows further reduction of high-scattering regions and optimal echo suppression, demonstrating the excellent radar-stealth performance [64]. And the FeCoNiMn@CNRs-3 sample exhibits even lower RCS values, reduced by 39.59 dBm^2 and 37.06 dBm^2 at 48° and 64° (Figure S10), respectively. Furthermore, the material's antibacterial activity against *E. coli* is also evaluated. The

Just Accepted

results (Figure 7b) show that the colonies in the blank control group (CK) were dense and evenly distributed. The number of colonies is drastically reduced in the experimental group when treated with the FeCoNiMn@CNRs-3 sample. The designed FeCoNiMn@CNRs-3 exhibits an exceptionally strong antibacterial effect, with a bacteriostatic rate approaching 100%. Based on previous studies and our results, the outstanding antibacterial performance of FeCoNiMn@CNRs-3 originates from two main mechanisms: (i) Its relatively high aspect ratio and rough surface significantly enhance the ability to capture bacteria, thereby penetrating them and allowing bacterial proteins and other substances to leak out [65]. This result was verified by measuring the absorbance of bacterial suspension at a wavelength of 280 nm, which yielded a value of 0.32 (Figure S11). (ii) The MA nanoparticles (FeCoNiMn) generate reactive oxygen species (ROS), which damage bacterial nucleic acid structures and deactivate the bacteria [61]. Its relative absorbance measured at 260 nm is 0.42, which aligns with our conclusions.

To further verify their reliabilities, the electrochemical tests on the corrosion resistance in a simulated seawater environment were performed [66]. The FeCoNiMn@CNRs-3 exhibited much higher open-circuit voltage values than those of FeCo@CNRs-3 and FeCoNi@CNRs-3 (Figure 7c). The Tafel curves in Figure 7d demonstrate that the corrosion potential (Ecorr) values follow the order: FeCoNiMn@CNRs-3>FeCoNi@CNRs-3>FeCo@CNRs-3. The corrosion current density (Icorr) can also be obtained according to the Tafel curve [67]. As summarized in Figure 7e, the acquired samples from FeCo@CNRs-3 to FeCoNi@CNRs-3 and FeCoNiMn@CNRs-3 present the progressively boosted Ecorr and decreased Icorr values, implying the evidently improved corrosion resistance in a simulated seawater environment [68]. In general, the outcomes confirm that the FeCoNiMn@CNRs-3

Just Accepted

simultaneously present the outstanding EM wave absorption performance, antibacterial activity and corrosion resistance.

On the basis of acquired results, the designed FeCoNiMn@CNRs-3 presents the outstanding EM wave absorbing, anti-corrosion, and antibacterial abilities, which originate mainly from the complementary mechanism formed at the microscopic level between the internal metal particles and the external carbon layer (as illustrated in Figure 7f). The 1D rod-like morphology forms a continuous conductive network, which facilitates the enhancement of conductive and interfacial polarization loss. Metal particles have a natural advantage in microwave absorption and have magnetic losses. At the same time, the surface of metal particles is rich in active sites and catalytic centers, which efficiently activates oxygen and water in the environment to continuously generate ROS [69]. On one hand, a heterojunction interface forms between metal and carbon layer, which generates the interface polarization [62]. On the other hand, it forms a natural barrier on the surface that effectively prevents external moisture, oxygen, and corrosive chloride ions from coming into direct contact with the metal. The higher aspect ratio of 1D structure greatly enhances its ability to capture bacteria and also extends the EM wave propagation path [63]. This functionally complementary core-shell design precisely satisfies the diverse and critical requirements for EM protection, environmental durability, and hygiene and safety across a wide range of application scenarios.

Just Accepted

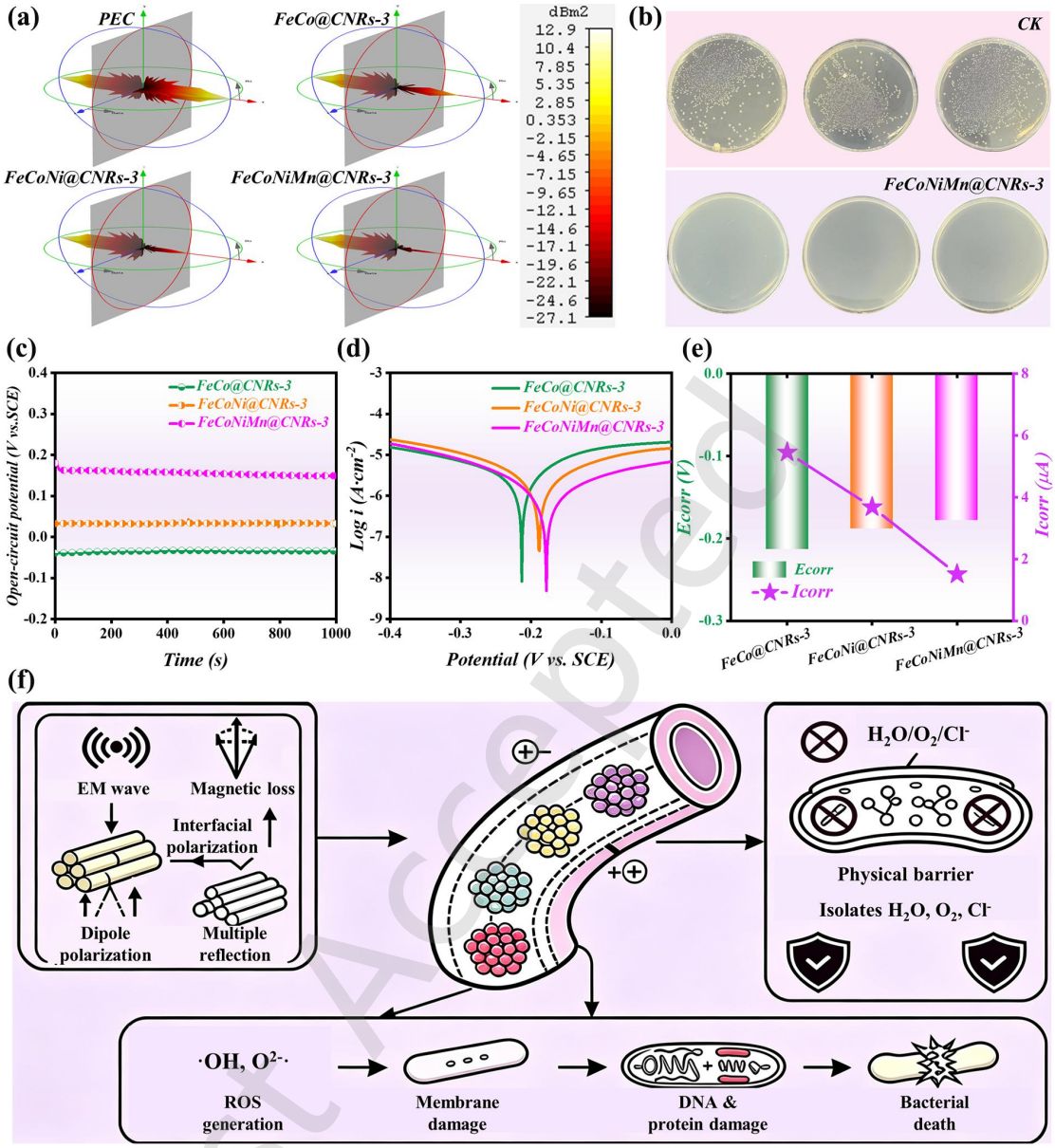


Figure 7. (a-e) RCS, antibacterial, and corrosion resistance results for FeCo@CNRs-3, FeCoNi@CNRs-3 and FeCoNiMn@CNRs-3, (f) diagram of the mechanisms for wave absorption, antibacterial action, and corrosion prevention of FeCoNiMn@CNRs-3.

Just Accepted

4. Conclusion

Using metal-NTAC NRs as precursors, 1D core@shell FeCo@CNRs, FeCoNi@CNRs and FeCoNiMn@CNRs with MA nanoparticles encapsulated in graphitic CNRs shell are efficiently and selectively produced through a continuous PR coating and thermal treatment. The study shows that the carbonization temperature from 900 to 1000 °C contributes to the progressively increased graphitization degree of outer CNRs layer, which significantly optimizes impedance matching and boosts both conduction and polarization loss. The optimized FeCoNi@CNRs present a superior RL_{min} of -52.57 dB and an EAB of 5.60 GHz. Furthermore, sequential incorporation of multiple metal components (Ni and Mn) further boosts their impedance matching and EM wave attenuation characteristics. Thanks to the unique structure and the synergistic effect of multiple components, the designed FeCoNiMn@CNRs simultaneously exhibit outstanding EMWAPs with the EAB of 6.4 GHz, strong antibacterial effect with a bacteriostatic rate approaching 100% and excellent corrosion resistance. The microscopic complementarity between the inner MA (magnetic loss and ROS catalysis) and outer carbon (interface polarization and physical barrier) underpins the triple-function synergy. Therefore, this study provides a facile, scalable, and composition-tunable metal-NTAC-derived strategy for designing 1D core@shell MA@CNRs as a novel multifunctional materials for microwave absorption, antibacterial protection, and corrosive-environment durability.

Just Accepted

ACKNOWLEDGEMENTS

The authors are grateful for the support from Guizhou Provincial Basic Research

Program (Natural Science) (No. ZD [2025] Key 086), Platform of Science and Technology and Talent Team Plan of Guizhou province (GCC[2023]007), Innovation Group of Guizhou University ([2024]08), Guizhou Provincial Basic Research Program (Natural Science) Youth Guidance Project (QN[2025]013) and Guizhou Provincial Major Scientific and Technological Program (XKBF(2025)010) for financial support.

CONFLICT OF INTEREST

The authors declare no conflict of interest.

CREDIT AUTHOR STATEMENT

Huirong Li and Hemin Wang: Investigation, Data curation, Writing-Original draft preparation. They contributed equally to this work. Junxiong Xiao: Investigation, Data curation, Visualization. Xin Gao: Methodology, Visualization. Beibei Zhan: Visualization, Investigation. Xiu Gong: Methodology, Visualization. Qiong Peng: Methodology, Visualization. Xiaosi Qi: Methodology, Visualization, Investigation, Writing-Reviewing and Editing.

REFERENCES

[1] Qi, J. M.; Liang, C. B.; Ruan, K. P.; Li, M. K.; Guo, H.; He, M. K.; Qiu, H.; Guo, Y. Q.; Gu, J. W. Cactus-like architecture for synergistic microwave absorption and thermal management. *Natl. Sci. Rev.* **2025**, *12*, nwaf394.

[2] Zhang, W. L.; Zhao, C.; Lan, D.; Xu, X. L.; Jia, Z. R.; Xu, X. Z. Enhanced interface polarization and optimized impedance matching in MoS_2/ZrO_2/CF

Just Accepted

composite for microwave absorption. *Carbon* **2026**, *257*, 121698.

[3] He, M. K.; Hu, J. W.; Yan, H.; Zhong, X.; Zhang, Y. L.; Liu, P. B.; Kong, J.; Gu, J. W. Shape anisotropic chain-like CoNi/polydimethylsiloxane composite films with excellent low-frequency microwave absorption and high thermal conductivity. *Adv. Funct. Mater.* **2025**, *35*, 2316691.

[4] Fang, G.; Liu, C. Y.; Xu, M.; Zhang, X. H.; Wu, Y.; Kim, D. H.; Ji, G. B. The elaborate design of multi‐polarization effect by non‐edge defect strategy for ultra-broad microwave absorption. *Adv. Funct. Mater.* **2024**, *34*, 2404532.

[5] Cheng, S. Y.; Chen, Z. L.; Sheng, D. H.; Dong, W.; Cao, R.; Su, Z. B.; Wu, M. D.; Zhu, X. F.; Xie, A. M.; Mukherjee, S. Y. et al. Sustainable electromagnetic interference shielding materials from cellulose-grafted *n*-type polymers. *Nat. Commun.* **2025**, *16*, 8608.

[6] Chen, Y. J.; Liu, Y. X.; Yang, X.; Wen, L. C.; Li, H. F.; Shang, H. C.; Cheng, S. Y.; Dong, W.; Xie, A. M. Dielectric response of specific N configurations in N-doped carbon enables efficient electromagnetic wave absorption. *Acta Phys.-Chim. Sin.* **2026**, *42*, 100379.

[7] He, M. K.; Gu, J. W. Tunable low-frequency microwave absorption and thermal management through in-situ confined growth of alloys within aramid nanofibers. *Eng. Tm.* **2026**, *1*, 150-163.

[8] Gu, W. H.; Ong, S. J. H.; Shen, Y. H.; Guo, W. Y.; Fang, Y. T.; Ji, G. B.; Xu, Z. J. A lightweight, elastic, and thermally insulating stealth foam with high infrared-radar compatibility. *Adv. Sci.* **2022**, *9*, 2204165.

Just Accepted

[9] Wu, Z. C.; Cheng, H. W.; Jin, C.; Yang, B. T.; Xu, C. Y.; Pei, K.; Zhang, H. B.; Yang, Z. Q.; Che, R. C. Dimensional design and core–shell engineering of nanomaterials for electromagnetic wave absorption. *Adv. Mater.* **2022**, *34*, 2107538.

[10] Liu, S.; Zhou, D. F.; Huang, F.; He, M.; Qin, S. H.; Shi, Y. Q.; Song, P. A. Heterointerface engineering of polymer-based electromagnetic wave absorbing materials. *Soft Sci.* **2025**, *5*, 7.

[11] Zhao, J.; He, M. K.; Guo, H.; Zhang, Y. L.; Qiu, H.; Lai, H. R. Multidimensional construction of 1T-MoS_2@graphene nanosheets nanocomposites for enhanced electromagnetic wave absorption. *J. Mater. Sci. Technol.* **2025**, *218*, 35-44.

[12] Tan, D. L.; Xu, C. H.; Chen, G. N.; Zhang, N. N.; Song, L. M.; Zhu, Y. Q.; Wang, H. L.; Zhang, F.; Zhang, R.; Fan, B. B. Charge-transfer states disclosed by first-principles calculations in core-shell carbon fiber@Ni and exploration of its microscopic electromagnetic loss mechanism. *Carbon* **2025**, *234*, 119931.

[13] Liu, Z. Y.; Huo, L. P.; Sun, Z. Y.; Wu, J. F.; Zhang, B. L. Raspberry-structured composite microspheres with enhanced electromagnetic wave attenuation via controlling the carbothermal process. *Sci. China Mater.* **2025**, *68*, 4192-4203.

[14] Guan, J. L.; Li, H. M.; Ren, J. N.; Qiu, W. H.; Li, Q.; He, Z. F.; Zhu, M. W.; Li, W.; Jia, N.; Lu, S. W. MOFs-derived flower-like cobalt@carbon multiscale hierarchical composites with effective microwave absorption in the low frequency range. *Int. J. Miner. Metall. Mater*. **2025**, *32*, 954-963.

[15] Wu, G. R.; Zhu, J. H.; Guo, X. M.; Zhang, C. M.; He, M. T.; Qiu, H.; Ma, D. W.

Just Accepted

Construction of Schottky barrier and the enhanced interface polarization effect of C@ZnO/Sn@GaN for high performance electromagnetic wave absorption. *Acta Phys.-Chim. Sin.* **2026**, *42*, 100324.

[16] Tong, Y. H.; Xu, H.; Zhang, B. G.; Xu, A. N.; Cao, R. C.; Xia, Y. F.; Chen, X.; Jin, H. Binder-induced interfacial engineering of a dual-layered SEI for durable silicon anodes over a wide temperature range. *Adv. Funct. Mater.* **2026**, *36*, e77501.

[17] Wang, H. M.; Xiao, J. X.; Wu, Y. Z.; Yang, Z. Q.; Kan, X. C.; Ding, J. F.; Zhang, Z. Q.; Zhang, X. K.; Qi, X. S. Modulation of built-In electric fields via doping strategy for efficient electromagnetic response. *Adv. Funct. Mater.* **2026**, *36*, e76998.

[18] Wen, L. C.; Cheng, S. Y.; Shang, H. C.; Sheng, D. H.; Li, W. J.; Qi, X. S.; Xie, A. M. Regulating interfacial strain from tensile to compressive state in transition-metal-sulfides/carbon for high-performance electromagnetic wave absorption. *Adv. Funct. Mater.* **2026**, *37*, e74621.

[19] Tao, J. Q.; Zou, K. X.; Zhou, J. T.; Wu, H. J.; Xu, L. L.; Wang, J.; Tao, X. W.; Huang, H. X.; Yao, Z. J. Phenolic multiple kinetics-dynamics and discrete crystallization thermodynamics in amorphous carbon nanostructures for electromagnetic wave absorption. *Nat. Commun.* **2024**, *15*, 10337.

[20] Gong, X. F.; Yao, L.; Ding, J. F.; Xie, A. M.; Qu, Y. P.; Tang, J. H.; Yang, W. B.; Zhang, Z. Q.; Qi, X. S. Metal-chelate derived strategy to produce CoNiFeMnCu@C high-entropy core@Shell nanorods for microwave absorption,

Just Accepted

anticorrosion and antibacterial properties. *Nano-Micro Lett*. **2026**, 10.1007/s40820-026-02401-7.

[21] Yao, L.; Dang, J.; Xiao, J. X.; Chen, Y. L.; Ding, J. F.; Qu, Y. P.; Peng, Q.; Qi, X. S.; Zhong, W. Metal chelate-derived and catalytical strategy to produce CoFe/C@bamboo-like carbon nanotubes for microwave absorption, hydrophobicity, and corrosion resistance. *J. Mater. Sci. Technol.* **2026**, *240*, 190-200.

[22] Zhao, X. Q.; Yun, K. L.; Zeng, X. J.; Wang, B.; Huang, R.; Tian, K. H.; Shu, R. W. Multi-level heterogeneous core-shell NRGO/$MgFe_2O_4$@SiO_2 composite for efficient microwave absorption and corrosion resistance via SiO_2 modulation. *Carbon* **2026**, *260*, 121954.

[23] Li, M. R.; Zhao, K. Y.; Fan, B. B.; Li, Y.; Tan, D. L.; Wang, H. L.; Gao, Q. L.; Li, W.; Zhang, H. S.; Zhu, Y. Q. et al. Rational A-site entropy engineering in perovskites: Dual-exchange enhanced magnetoelectric coupling for ultra-efficient microwave absorption. *Adv. Sci.* **2026**, *13*, e16938.

[24] Xu, S.; Jia, Z. R.; Lan, D.; Shi, M. J.; Gao, Z. G.; Wu, G. L. Synergistic polarization relaxation in multi-level hybridization and preferred orientation strategies for electromagnetic wave absorption. *Adv. Funct. Mater.* **2026**, *36*, e75567.

[25] You, Q.; Zhao, Y. Q.; Zhong, Y.; Xu, F. H.; Zhang, X. F.; Cui, S. Novel PRSi/AlN aerogel composites enabled synergistic thermal insulation and microwave absorption by sealing enhancement strategy and spontaneous ceramization. *Adv.*

Just Accepted

Compos. Hybrid Mater. **2026**, *9*, 325.

[26] Chen, L. H.; Pan, J. J.; Wang, T.; Xia, W.; He, J. P.; Zhang, K. 1D magnetic nickel-carbon matrix nanotube composites derived from hydrogen-bonded organic frameworks and metal–organic frameworks for electromagnetic wave absorption. *Adv. Funct. Mater.* **2025**, *35*, 2409432.

[27] Xu, Z. J.; Wang, B. J.; Li, L.; Ma, W. L.; Che, R. C.; Zhang, H. Ultralight medium-entropy alloy/CNT aerogels with synergistic magnetoelectric coupling for enhanced low-frequency microwave absorption. *Adv. Funct. Mater.* **2026**, *36*, e77003.

[28] Wei, M.; Fan, H. B.; Yu, F. J.; Qiu, Z.; Xiao, Z. F.; Zhang, T. P.; Xie, Y. J. A "three birds with one stone" strategy: Ni_3Fe-decorated carbonized wood composites for high-performance and multifunctional electromagnetic interference shielding. *Adv. Compos. Hybrid Mater.* **2026**, *9*, 307.

[29] Sun, R.; Lv, H. W.; Lian, G. J.; Wang, L.; Huang, M. Q.; You, W. B.; Che, R. C. Dielectric shell regulation in synergy FeCoNi@$ZnIn_2S_4$ microspheres with broadband electromagnetic wave absorption. *Soft Sci.* **2025**, *5*, 35.

[30] Cui, K. B.; He, C. L.; Wu, J. H.; Gao, X.; Li, Y.; Han, P.; Sun, N. N.; Wang, Y. F.; Hao, X. H.; Li, L. et al. Multispectrum electromagnetic response in FeNiHo/C heterodimensional structure for microwave absorption and multimode photodetection. *Adv. Mater.* **2025**, *37*, e10507.

[31] Li, L. W.; Ban, Q. F.; Song, Y. J.; Liu, J.; Qin, Y. S.; Zhang, T. T.; Kong, J. Self-templating engineering of hollow N-doped carbon microspheres anchored

Just Accepted

with ternary FeCoNi alloys for low-frequency microwave absorption. *Small* **2024**, *20*, 2406602.

[32] Zhou, X. Y.; Wu, X. H.; Li, S. Y.; He, Y.; Wang, R. Q.; Rao, S. Y.; Zhuang, Q. X.; Zhou, Y. K.; Liu, X. Y.; Zuo, P. Y. The cation exchange driving multi-phase regulation in Co_7Fe_3/Co@NC for enhanced broadband electromagnetic wave absorption. *Carbon* **2024**, *230*, 119592.

[33] Rao, L. J.; Wang, L.; Yang, C. D.; Zhang, R. X.; Zhang, J. C.; Liang, C. Y.; Che, R. C. Confined diffusion strategy for customizing magnetic coupling spaces to enhance low-frequency electromagnetic wave absorption. *Adv. Funct. Mater.* **2023**, *33*, 2213258.

[34] Xiao, J. X.; Zhan, B. B.; Tan, Z. Y.; Ding, J. F.; Qu, Y. P.; Gong, X.; Peng, Q.; Zhong, W.; Chen, Y. L.; Qi, X. S. Integration of photo-driven rapid self-healing and environmental robustness for durable electromagnetic wave absorbing elastomers. *InfoMat* **2026**, *8*, e70127.

[35] Li, X.; Wang, X. L.; Li, M. H.; Zhu, W. J.; Luo, H. J.; Lu, X. K.; Xu, H. L.; Xue, J. M.; Ye, F.; Wu, H. J. et al. Built-in electric field enhancement strategy induced by cross-dimensional nano-heterointerface design for electromagnetic wave absorption. *Adv. Funct. Mater.* **2025**, *35*, 2407217.

[36] Tian, Z. N.; Liu, J. Y.; Zhang, M.; Jia, Q. Q.; Liu, M. B.; Li, Z. J.; Wang, T.; Zhao, W. J.; Ma, D. W.; Qi, X. L. Constructing selenium-vacancy-rich SiC@$CoSe_{2-x}$ nanocomposites to boost dipole and interfacial polarization for electromagnetic wave absorption. *Acta Phys.-Chim. Sin.* **2026**, *42*, 100323.

Just Accepted

[37] Wu, P. K.; Tan, S. J.; Yan, X.; Ning, Y.; Yang, R. P.; Shen, L. F.; Zheng, J.; Ji, G. B. Ionogel enhanced by molecular structure engineering and microphase separation synergy for broadband microwave absorption and light-controlled thermal management. *Adv. Funct. Mater.* **2026**, *36*, e32154.

[38] Wang, P. W.; Bian, L. J.; Jiang, J. Y.; Zhao, P. Z.; Wang, X. J.; Xie, L. Y.; Tong, G. X.; Wu, W. H. Constructing dual networks in tissue-paper-derived carbon nanofiber/Co@C composites toward exceptional microwave absorption and heat conduction. *Carbon* **2026**, *251*, 121305.

[39] Li, S. Z.; Xie, T. W.; Ma, L.; Lei, Z. X.; Huang, N.; Song, H.Z.; Feng, Y. H.; Li, B.; Cui, Y.; Liu, L. et al. Ni_3Fe@N-doped carbon nanotubes 3D network induced by nanoconfined symmetry breaking for high-performance microwave absorption, corrosion protection, and pollutant purification. *Carbon* **2023**, *213,* 118302.

[40] Zhan, B. B.; Zhang, Y. R.; Tan, Z. Y.; Xie, A. M.; Gong, X.; Peng, Q.; Yang, J. L.; Qu, Y. P.; Qi, X. S. Multi-dimensional, multi-interfacial, and multi-path synergy enables broadband absorption, corrosion resistance, Joule heating, and thermal performances in hierarchical carbon/Ni nanoparticles-carbon nanocoils foams. *InfoMat* **2026**, *8*, e70098.

[41] Wang, J. L.; Qu, H. C.; Ye, X. Y.; Tan, S. J.; Yan, X.; Li, P. Z.; Tian, W. Z.; Ji, G. B. Electronic structure and absorption mechanism of Fe-doped $Y_{0.9}Sr_{0.1}CoO_3$ perovskite microwave absorbers. *J. Adv. Ceram.* **2025**, *14*, 9221191.

[42] Xu, S.; Jia, Z. R.; Lan, D.; Gao, Z. G.; Zhang, S. Y.; Wu, G. L. Synergistic polarization relaxation in heteroatom-optimized heterointerfaces for

Just Accepted

electromagnetic wave absorption. *Adv. Funct. Mater.* **2025**, *35*, 2500304.

[43] Zhao, J.; Gu, Z.; Liu, J. H.; Yu, Y. Q.; Zhang, Y. K.; Li, M. Rational construction of laver-derived carbon@MoS_2 nanocomposites with superior electromagnetic wave absorption and electrochemical performances. *J. Mater. Sci. Technol.* **2026**, *274*, 160-168.

[44] Zhao, J.; Yu, Y. Q.; Gu, Z.; Zhang, Y. K.; Wang, D. S. Superior electromagnetic wave absorption of wood chips-derived carbon@MoS_2 composites with photocatalytic hydrogen evolution function. *Acta Phys.-Chim. Sin.* **2026**, 100366, 10.1016/j.actphy.2026.100366.

[45] Zhang, H.; Wang, J. E.; Zhang, Y. L.; Meng, Y. T.; Xue, Y. H.; Liu, Z.; Liang, B. L.; Gu, J. W. MoS_2 Nanoflower-Mediated MXene/ANF Composite Films with Simultaneous Strength-Toughness Synergy and High-Efficient Electromagnetic Interference Shielding. *Adv. Funct. Mater.* **2026**, 10.1002/adfm.78516.

[46] Hou, H. Y.; Ma, D. W.; Zhang, Z. N.; Jia, Z. R. Synergistic mechanism and performance optimization of dielectric-magnetic composite absorbing material. *Acta Phys.-Chim. Sin.* **2026**, *42*, 100325.

[47] Liu, Z.; Xue, Y. H.; Meng, Y. T.; Wang, J. E; Zhang, H.; Zhang, F. J.; Meng, F. B.; Zhao, B.; Yan, L. T.; Liang, B. L. Reduced-reflectance bionic E-Skin with electromagnetic–environmental–sensing integration enabled by Ni-reconstructed liquid metal networks. *Adv. Funct. Mater.* **2026**, e76178, 10.1002/adfm.76178.

[48] Zhu, L. S; Cui, C. Y.; Jing, T.; Tan, S. H.; Liu, X. G.; Yu, M. L. Strong and broadband microwave absorption under thin thickness induced by multiple

Just Accepted

dielectric relaxation and multiple magnetic resonances through the dual nanocrystalline phases in amorphous FeSiBCr flakes. *Acta Phys.-Chim. Sin.* **2026**, *42*, 100331.

[49] Cheng, J. Y.; Chen, Q. K.; Wang, H. H.; Jin, Y. H.; Jiang, S. H.; Xie, B. L.; Wang, Y. F.; Zheng, H. M.; Liu, B.; Wu, C. et al. Engineering dielectric genes in debye relaxation model toward frequency-band-reliant electromagnetic responses. *Adv. Mater.* **2026**, *38*, e21471.

[50] Yang, S. H.; Guo, Z. Q.; Jia, Z. R.; Liu, Y.; Wang, D. S.; Li, Z. C.; Li, H. F.; Qiu, H.; Wu, G. L. Precisely engineered heterointerfaces in bimetallic MOFs enable multiscale polarization synergy for efficient electromagnetic attenuation. *Acta Phys.-Chim. Sin.* **2026**, *42*, 100348.

[51] Li, Y. X.; Liao, Y. J.; Ji, L. Z.; Hu, C. L.; Zhang, Z. H.; Zhang, Z. Y.; Zhao, R. Z.; Rong, H. W.; Qin, G. W.; Zhang, X. F. Quinary high-entropy-alloy@graphite nanocapsules with tunable interfacial impedance matching for optimizing microwave absorption. *Small* **2022**, *18*, 2107265.

[52] Yang, B. T.; Fang, J. F.; Xu, C. Y.; Cao, H.; Zhang, R. X.; Zhao, B.; Huang, M. Q.; Wang, X. Y.; Lv, H. L.; Che, R. C. One-dimensional magnetic FeCoNi alloy toward low-frequency electromagnetic wave absorption. *Nano-Micro Lett.* **2022**, *14*, 170.

[53] Wang, B. Q.; Xu, Y.; Deng, C. W.; Ye, Q. B.; Li, L. C.; Jiang, X. Y.; Zhou, T. D. Rare-earth doped high-entropy alloys with gradient architectures for low-frequency ultra-broadband electromagnetic wave absorption. *J. Rare Earths*

Just Accepted

2026, 10.1016/j.jre.2026.07.003.

[54] Huang, L. T.; Bai, C. H.; Jia, J. Y.; Chen, Y. J.; Zhu, C. L.; Ma, X. Z.; Zhang, X. Rapid joule-heating-driven synthesis of FeCo alloy nanoparticles embedded in porous carbon nanorods for electromagnetic wave absorption. *Carbon* **2025**, *243*, 120592.

[55] Gang, S. F.; He, H.; Long, H.; Wei, Y. C.; Zhang, W. G.; Li, X.; Qian, Y. X.; Luo, Y. B.; Yang, J. Y. 2D-high entropy alloys embedded in 3D-carbon foam towards light-weight electromagnetic wave absorption and hydrophobic thermal insulation. *Nano Energy* **2025**, *135*, 110642.

[56] Hao, J. C.; Zhuang, Z. C.; Cao, K. C.; Gao, G. H.; Wang, C.; Lai, F. L.; Lu, S. L.; Ma, P. M.; Dong, W. F.; Liu, T. X. et al. Unraveling the electronegativity-dominated intermediate adsorption on high-entropy alloy electrocatalysts. *Nat. Commun.* **2022**, *13*, 2662.

[57] Lv, F. Y.; Wang, Y. Q.; He, Q. C.; Lan, D.; Wu, G. L. High-entropy strategy-driven lattice distortion and electronic rearrangement in MOF-derived HEA/NC composites for balanced electromagnetic response and superior microwave attenuation. *Adv. Funct. Mater.* **2026**, *36*, e75416.

[58] Zhou, X. Y.; Jiang, Z.; Li, Y. F.; Wang, R. Q.; Sun, Y. R.; Dai, S. K.; Zhuang, Q. X.; Fang, J. Y.; Qian, J.; Zuo, P. Y. Nanoscale dielectric gene dual-regulations in high-entropy materials for enhanced electromagnetic wave absorption over low-mid frequency. *Small* **2026**, *22*, e73822.

[59] Liu, X. J.; Duan, Y. P.; Wu, N.; Li, G. M.; Guo, Y.; Liu, J. Y.; Zhu, N.; Wang, Q.;

Just Accepted

Wang, L.; Xu, Z. C. et al. Modulating electromagnetic genes through bi-phase high-entropy engineering toward temperature-stable ultra-broadband megahertz electromagnetic wave absorption. *Nano-Micro Lett.* **2025**, *17*, 164.

[60] Duan, Y. P.; Li, M. Q.; Guo, Y.; Zhu, N.; Pang, H. F.; Dou, C. X. Improving electromagnetic wave absorption performance by adjusting the proportion of brittle BCC phase in FeCoNiCr0.4Mnx high-entropy alloys. *Today Phys.* **2024**, *49*, 101596.

[61] Xu, H. S.; Xue, Q. Z.; An, X. P.; Zheng, L. C.; Huang, H. F.; Nan, K.; Wang, Y. Multi-level defect engineering combining heterointerfaces, vacancies, and heteroatoms for microwave absorption and antibacterial activity. *Carbon* **2026**, *260*, 121953.

[62] Bai, J. X.; Li, L. Y.; Pei, K.; Cao, Q.; Yuan, X. Z.; Jiang, M.; Ma, Z.; Che, R. C.; Cao, M. S. Dielectric gene tailoring and interfacial polarization relaxation in Mo-Fe bimetallic carbide for low‐frequency electromagnetic response. *Adv. Funct. Mater.* **2026**, *36*, e24804.

[63] Tian, K. H.; Yang, H.; Zhang, C.; Shu, R. W.; Shao, Q.; Liu, X. W.; Gao, K. P. Fabrication of flake-like $NiCo_2O_4$/reduced graphene oxide/melamine-derived carbon foam as an excellent microwave absorber. *Int. J. Miner. Metall. Mater.* **2025**, *32*, 556-565.

[64] Zhang, X.; Wang, H. Y.; Hao, Y. L.; Qu, Y. P.; Wang, X. H.; Jiang, W. Y.; Li, H. F.; Deng, C. Y.; Qi, X. S. Peanut biomimetic functional phases-engineered metacomposites with loading-insensitive epsilon-negative response for

Just Accepted

electromagnetic shielding. *Acta Phys.-Chim. Sin.* **2026**, *42*, 100326.

[65] Liang, Q. Q.; He, M. K.; Zhan, B. B.; Guo, H.; Qi, X. S.; Qu, Y. P.; Zhang, Y. L.; Zhong, W.; Gu, J. W. Yolk-shell CoNi@N-doped carbon-CoNi @CNTs for enhanced microwave absorption, photothermal, anti-corrosion, and antimicrobial properties. *Nano-Micro Lett.* **2025**, *17*, 167.

[66] Wei, Z. H.; Chen, X. Y.; Chen, D. W.; Liang, J.; Liao, Z. J.; Li, X. S.; Li, Z. C.; Kong, J. N and S dual doping and defect engineering to modulate electronic structure of 3D honeycomb-like carbon for boosting microwave absorption. *Carbon* **2025**, *233*, 119925.

[67] Hou, Y. L.; Liu, Z. Y.; Wang, Q.; Yu, Z.; Xing, R. Z.; Yu, Z. L.; Tang, Y. S.; Kong, J. Magnetic graphene composite aerogel for highly efficient electromagnetic wave absorption and anti-corrosion. *J. Mater. Sci. Technol.* **2026**, *251*, 1-10.

[68] Wang, J. E.; Ming, W.; Chen, L. F.; Song, T. L.; Yele, M. X.; Zhang, H.; Yang, L.; Sarula, G. G.; Liang, B. L.; Yan, L. T. et al. MoS_2 lubricate-toughened MXene/ANF composites for multifunctional electromagnetic interference shielding. *Nano-Micro Lett.* **2025**, *17*, 36.

[69] Yan, W. R.; Hu, J. X.; Yi, C.; Wang, Q. W.; Wang, J.; Zhang, W.; Huang, X. Y.; Liu, Y. N.; Gao, X.; Zeng, H. F. et al. Radial dielectric gradient core-shell Ce/NiCo@C composites for simultaneous electromagnetic wave absorption and antibacterial activity via Ce^{3+}/Ce^{4+} valence modulation. *Adv. Funct. Mater.* **2025**, *35*, 2501645.

Just Accepted

Electronic Supplementary Material

A universal NTA chelation-derived strategy to develop triple-functional core@shell magnetic carbon nanorods for microwave absorption, antibacterial, and anticorrosion applications

Huirong Li[§], Hemin Wang[§], Junxiong Xiao, Xin Gao, Beibei Zhan, Xiu Gong, Qiong Peng, and Xiaosi Qi*

College of Physics, Guizhou University, Guiyang 550025, China

[§]Huirong Li and Hemin Wang contributed equally to this work.

Address correspondence to xsqi@gzu.edu.cn

Supporting information to https://doi.org/10.26599/NR.2026.94909268

Just Accepted

2. Experimental Section

2.1. Characterization and Measurement

The samples were systematically analyzed to investigate their morphology, structure, composition, and chemical states through advanced techniques, including scanning electron microscopy (SEM), transmission electron microscopy (TEM), X-ray diffraction (XRD), Raman spectroscopy (Raman), and X-ray photoelectron spectroscopy (XPS). Electrochemical performance, particularly corrosion resistance, was assessed using a electrochemical workstation. Additionally, the electromagnetic properties were determined via a vector network analyzer utilizing the coaxial-line method. Furthermore, the annealing of the samples was performed in a tube furnace (model BTF-1200C-S, Anhui BEQ Equipment Technology Co., Ltd.).

Table S1. Experimental Procedures for the preparation of FeCo-NTAC, FeCoNi-NTAC and FeCoNiMn-NTAC**.**

$FeCl_2 \cdot 4H_2O$ (mmol)	**$CoCl_2 \cdot 6H_2O$ (mmol)**	**$NiCl_2 \cdot 6H_2O$ (mmol)**	**$MnCl_2 \cdot 4H_2O$ (mmol)**	**Categories of Metal-NTAC**
0.3	0.3	−	−	FeCo-NTAC
0.2	0.2	0.2	−	FeCoNi-NTAC
0.15	0.15	0.15	0.15	FeCoNiMn-NTAC

Table S2. Main conditions for the synthesis of FeCoNi@CNRs, FeCo@CNRs and FeCoNiMn@CNRs

Just Accepted

Precursor	Intermediate product	Temperature	Sample
FeCoNi-NTAC	FeCoNi-NTAC@PR	900 °C	FeCoNi@CNRs-1
FeCoNi-NTAC	FeCoNi-NTAC@PR	950 °C	FeCoNi@CNRs-2
FeCoNi-NTAC	FeCoNi-NTAC@PR	1000 °C	FeCoNi@CNRs-3
FeCo-NTAC	FeCo-NTAC@PR	1000 °C	FeCo@CNRs-3
FeCoNiMn-NTAC	FeCoNiMn -NTAC@PR	1000 °C	FeCoNiMn@CNRs-3

Just Accepted

Table S3. Comparison table about MAPs with the recently reported representative works.

Materials	EAB (GHz)	Thickness (mm)	RL_{min} (dB)	Thickness (mm)	Reference
CF@Ni-6	5.92	2.20	-49.87	2.10	[12]
C/Fe_3O_4@Fe_2SiO_4@DC	6.03	2.20	-17.86	2.20	[13]
Co@C/CF	3.24	1.50	-55.70	2.80	[14]
C@ZnO/Sn@GaN	6.32	2.20	-48.07	2.60	[15]
SAC-3	5.80	2.20	-45.90	1.88	[20]
FeCoNi@NCMs	5.34	1.70	-34.30	1.70	[31]
H-Co_7Fe_3/Co@NC	6.01	2.10	-59.70	3.00	[32]
FeCo@C-3	2.58	4.00	-35.90	4.00	[33]
Co/CeO_2@NC	5.10	1.90	-52.70	1.90	[61]
Mo_2C	3.44	2.50	-49.50	2.50	[62]
FNC/RGO/MDCF	3.84	1.50	-66.44	2.29	[63]
FeCoNiMn@CNRs-3	6.40	2.16	-19.72	1.92	This work

3. Equations:

$$\alpha = \frac{\sqrt{2}\pi f}{c}\sqrt{\left(\mu''\varepsilon'' - \mu'\varepsilon'\right) + \sqrt{\left(\mu''\varepsilon'' - \mu'\varepsilon'\right)^2 + \left(\varepsilon'\mu'' + \varepsilon''\mu'\right)^2}}$$

(S1)

Just Accepted

$$Z = \frac{Z_{in}}{Z_0} = \sqrt{\frac{\mu}{\varepsilon}} \tanh\left(j \frac{2\pi f d \sqrt{\mu\varepsilon}}{c} \right)$$

(S2)

$$RL = 20 \log \left| \frac{Z_{in} - Z_0}{Z_{in} + Z_0} \right| \quad \text{(S3)}$$

Where ε, μ, ε', ε'', μ', μ'', d, c, f, Z_0 *and* Z_{in} represent complex permittivity ($\varepsilon = \varepsilon' - j\varepsilon''$), complex permeability ($\mu = \mu' - j\mu''$), real and imaginary parts of complex permittivity, real and imaginary parts of complex permeability, thickness of sample, velocity of light, frequency of EM wave, impedance of air and input impedance of MAs, respectively.

Just Accepted

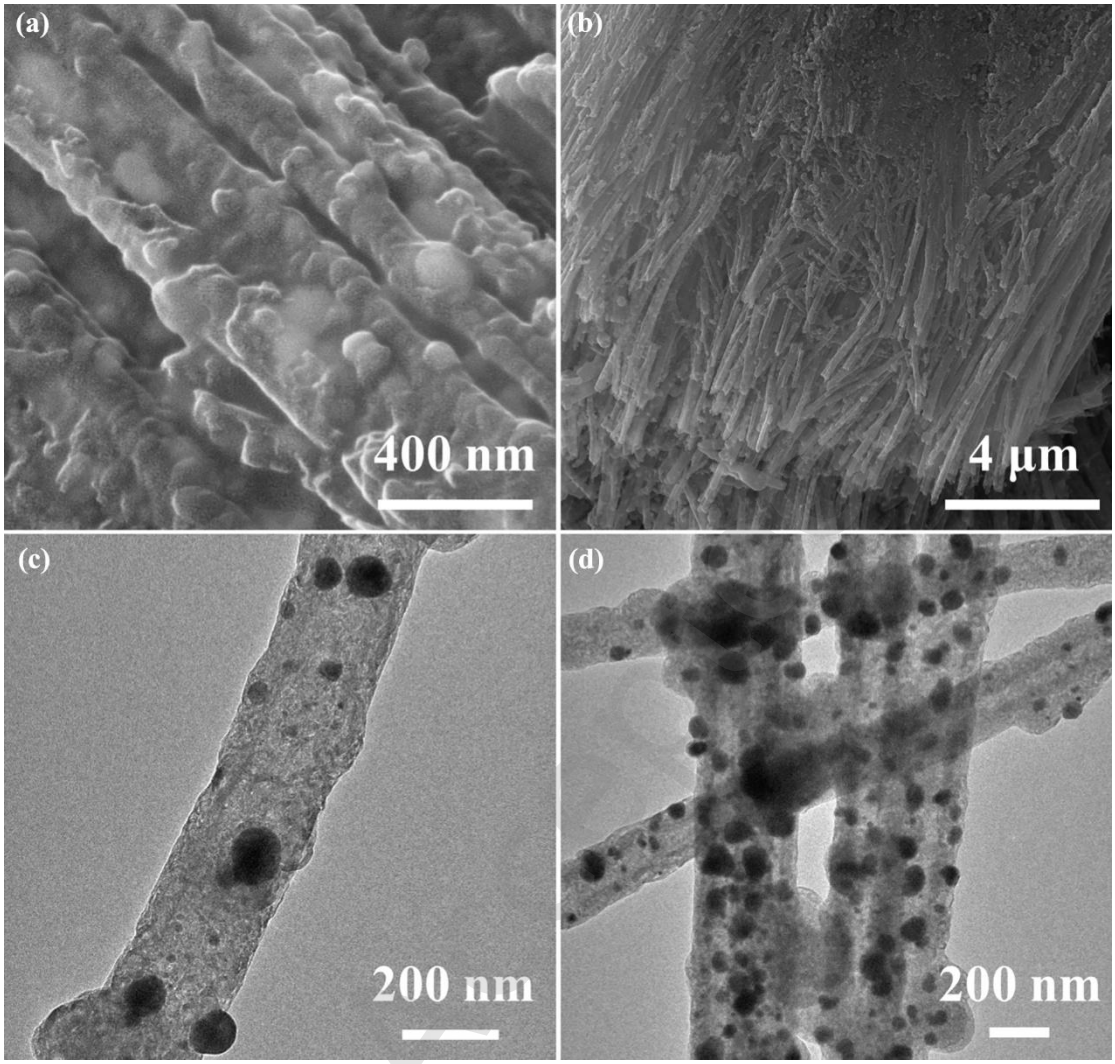


Figure S1. (a, b) Typical SEM and (c, d) TEM images of FeCoNi@CNRs-3.

Just A

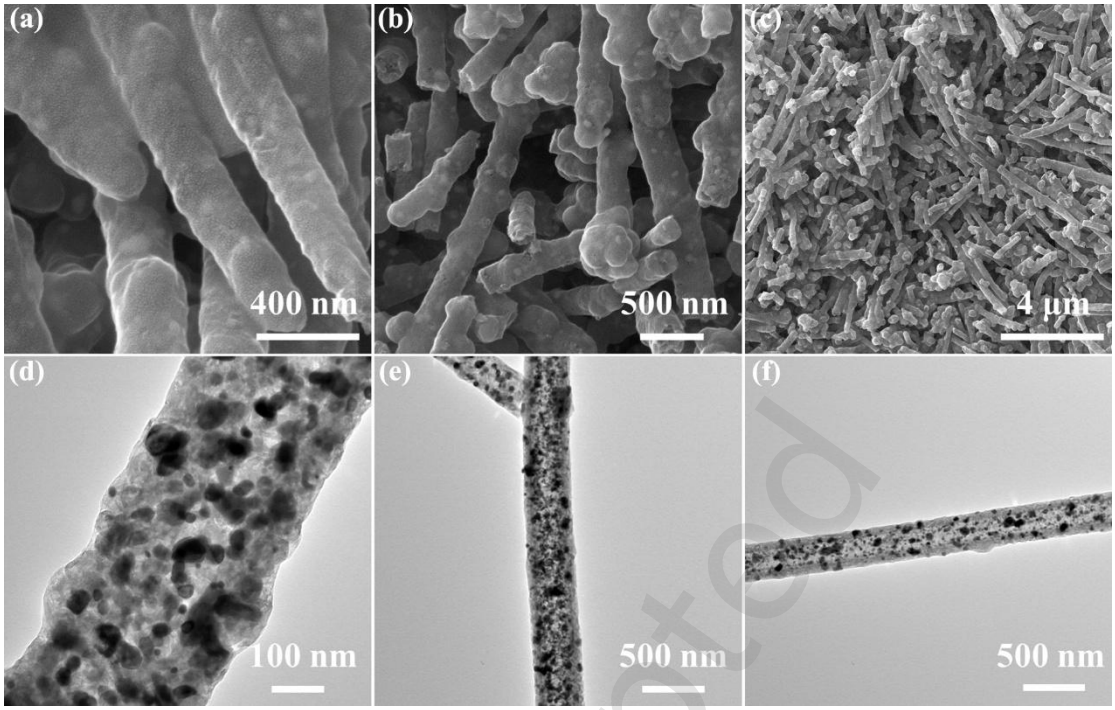


Figure S2. (a-c) SEM, (d-f) TEM images of FeCoNi@CNRs-1.

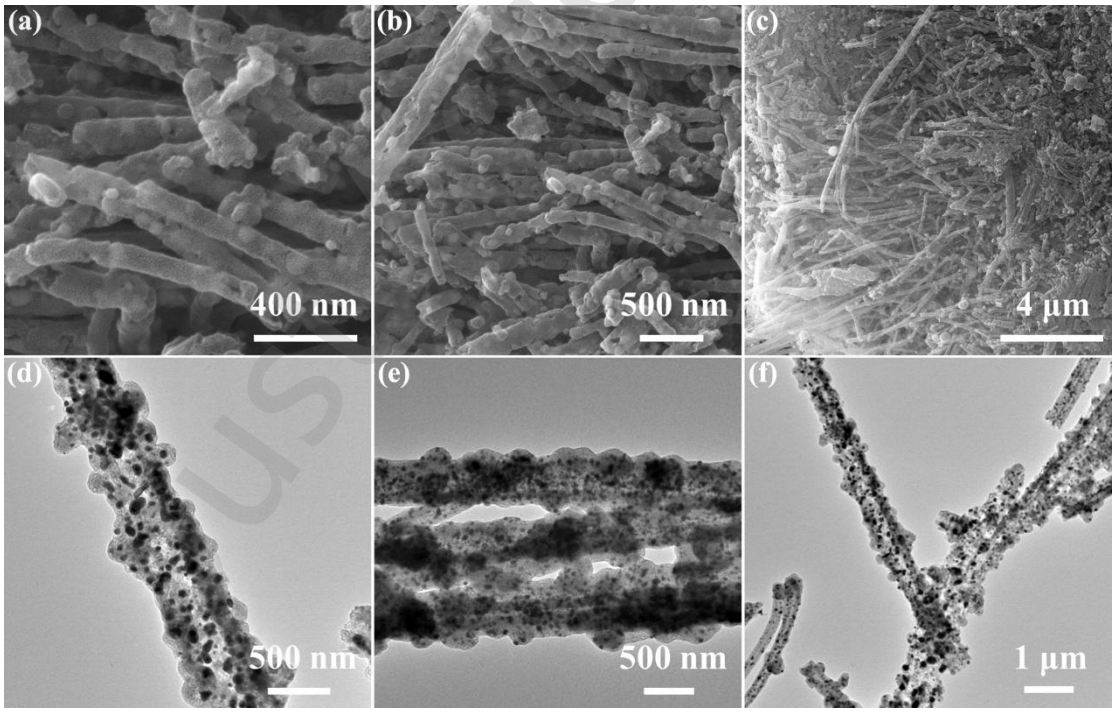


Figure S3. (a-c) SEM and (d-f) TEM images of FeCoNi@CNRs-2.

Accepted

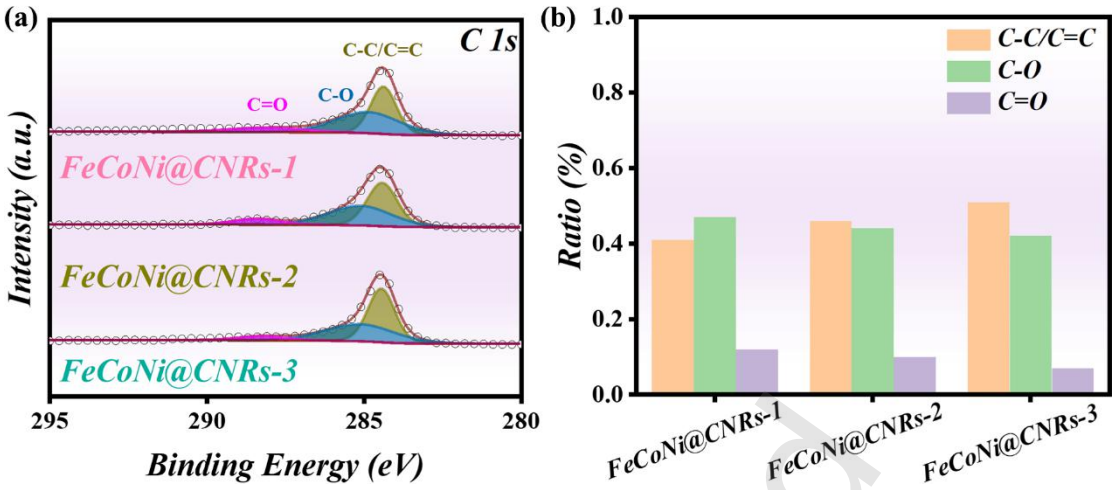


Figure S4. (a) C 1s spectra, (b) proportion of C–C/C=C, C–O, and C=O bond contents of FeCoNi@CNRs-1, FeCoNi@CNRs-2 and FeCoNi@CNRs-3.

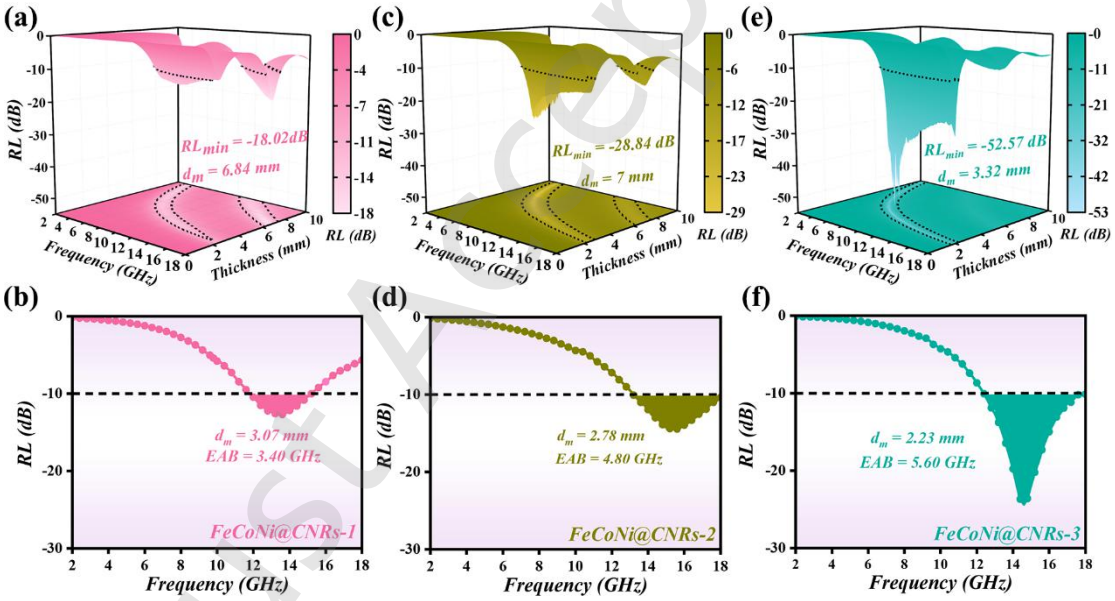


Figure S5. Typical three-dimensional and two-dimensional RL curves of (a, b) FeCoNi@CNRs-1, (c, d) FeCoNi@CNRs-2 and (e, f) FeCoNi@CNRs-3.

Just Accepted

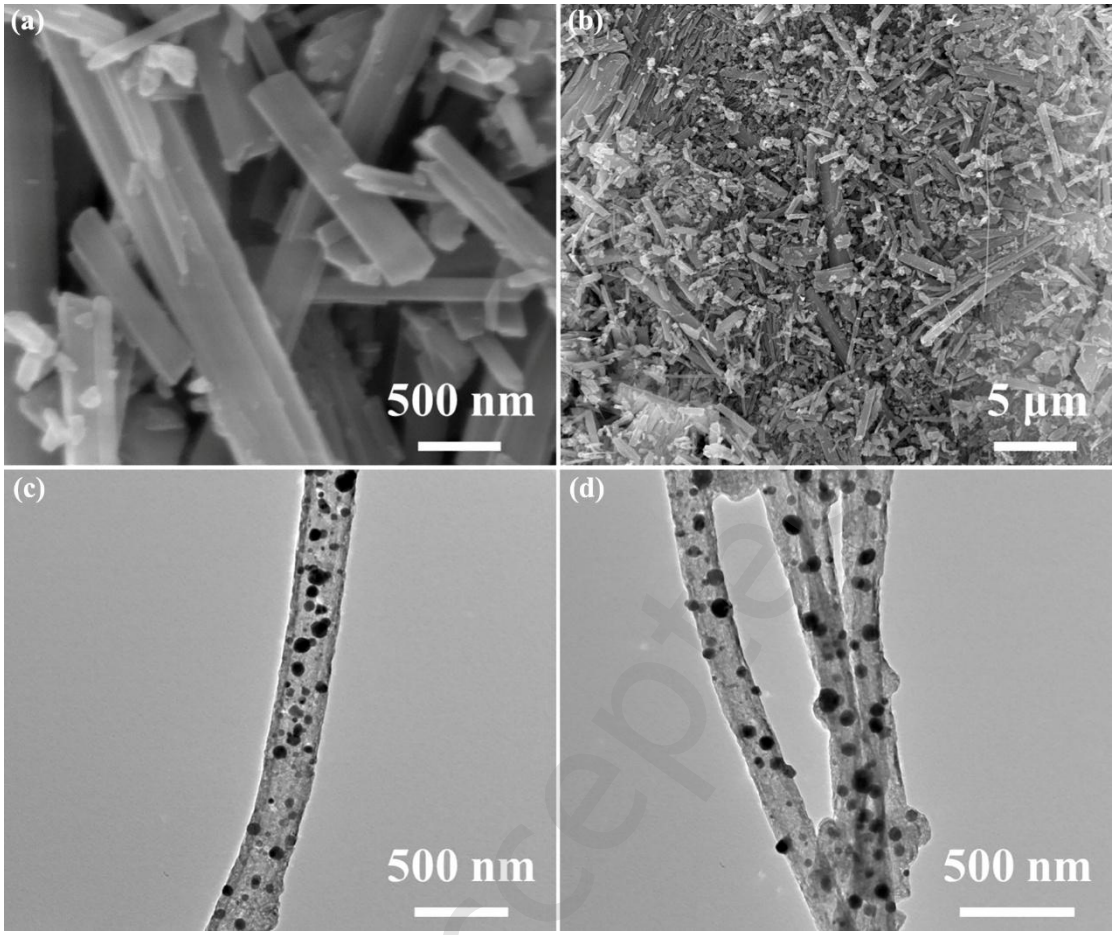


Figure S6. (a, b) Typical SEM and (c, d) TEM images of FeCo@CNRs-3.

Just Accepted

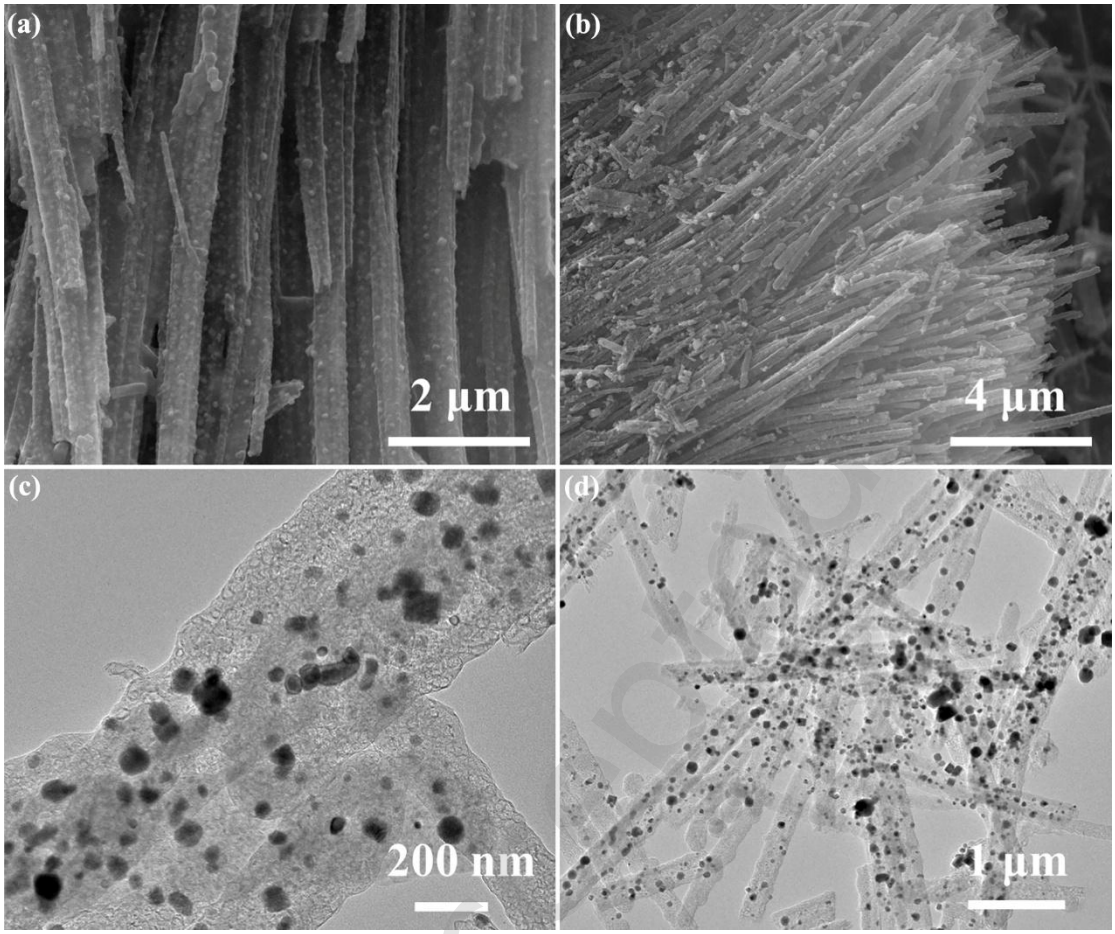


Figure S7. (a, b) SEM, (c, d) TEM images of FeCoNiMn@CNRs-3.

Just Accepted

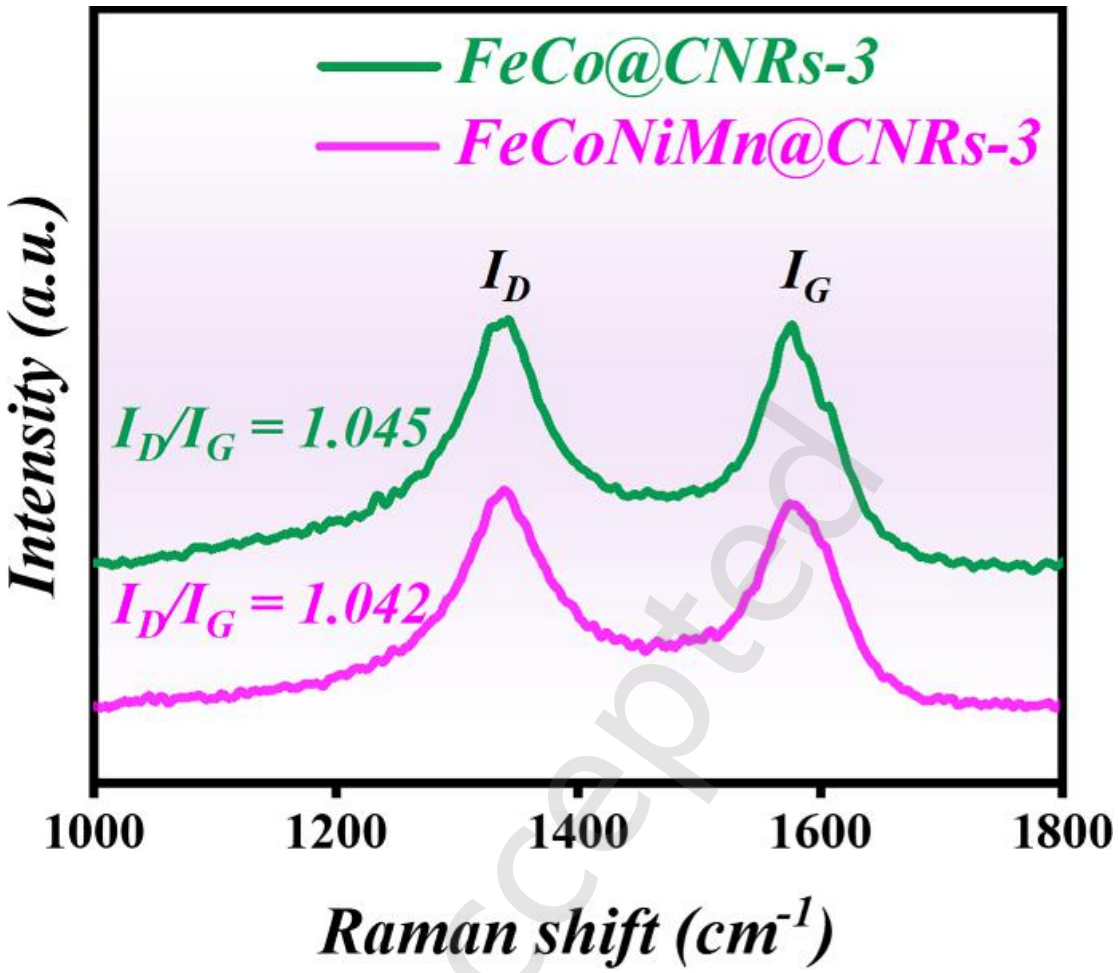


Figure S8. Raman diagram for FeCo@CNRs-3 and FeCoNiMn@CNRs-3.

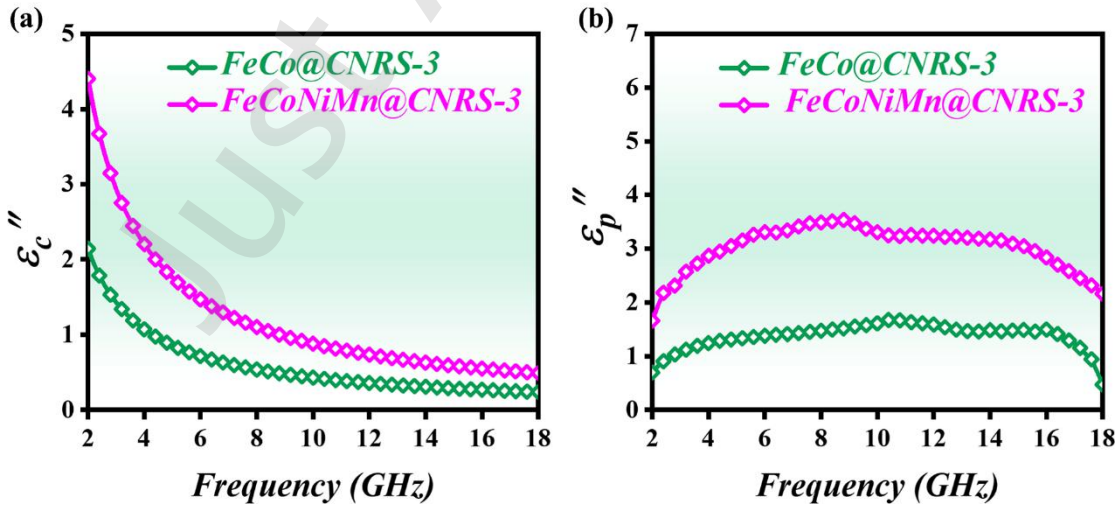


Figure S9. (a) $\varepsilon_c'' \sim f$ and (b) $\varepsilon_p'' \sim f$ curves for FeCo@CNRs-3 and FeCoNiMn@CNRs-3.

Just Accepted

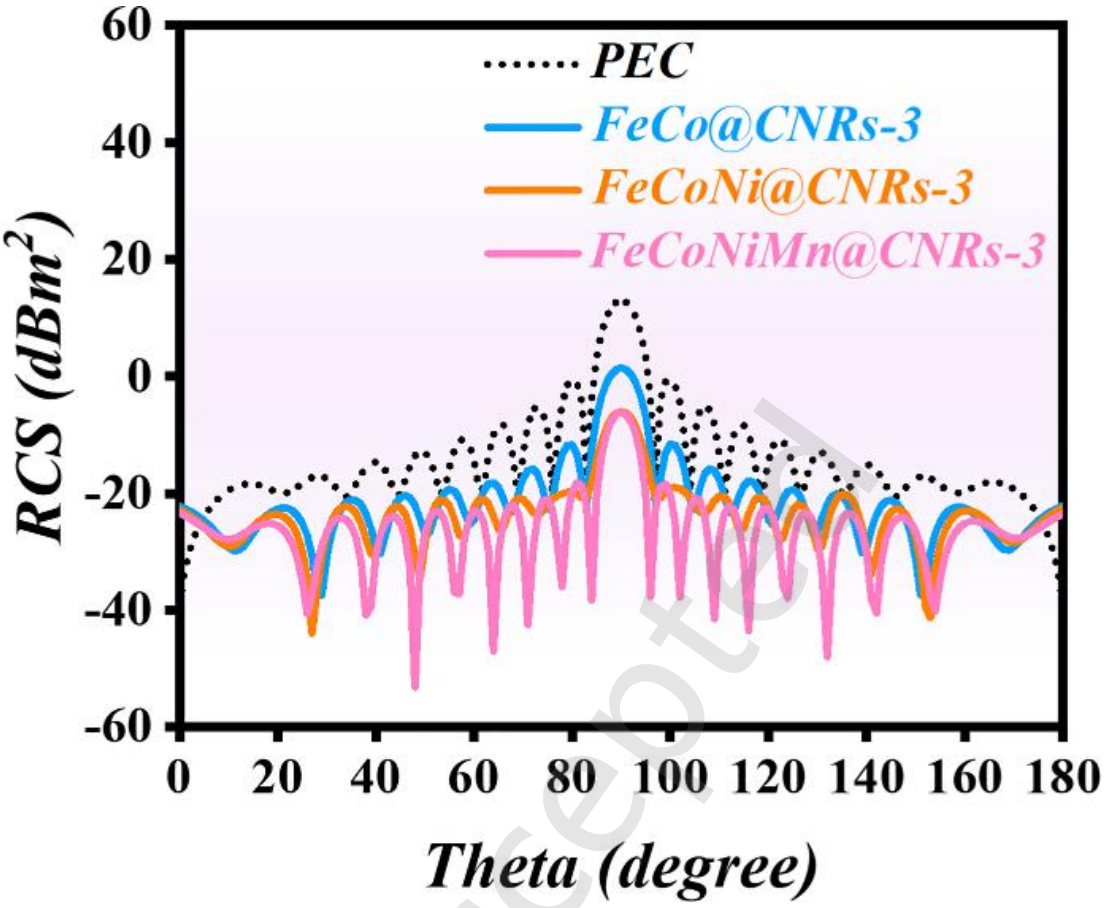


Figure S10. RCS simulation curves for FeCo@CNRs-3, FeCoNi@CNRs-3 and FeCoNiMn@CNRs-3.

Just Accepted

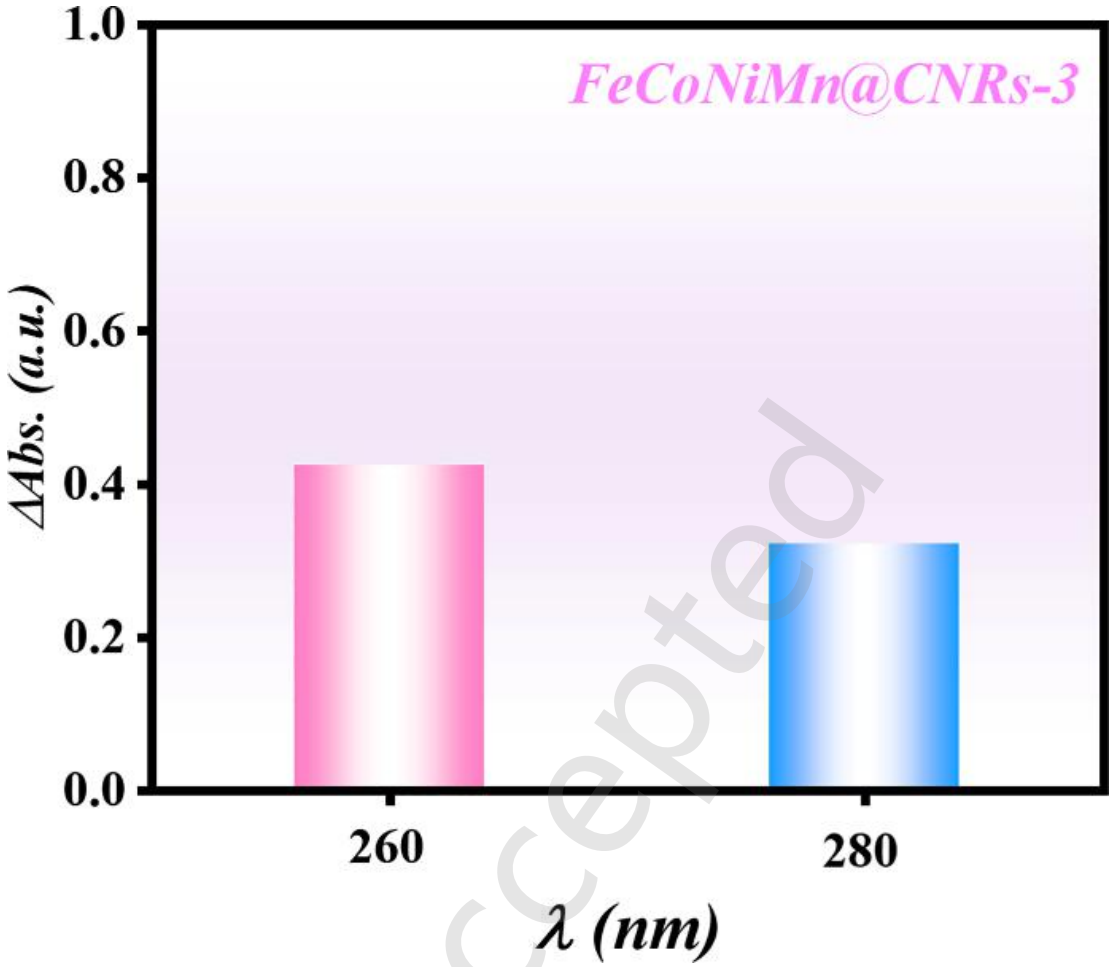


Figure S11. Optical Density value of FeCoNiMn@CNRs-3

Just Accepted